Material Matters™

ALDRICH®
Materials Science

Materials for Energy Harvesting and Storage

Innovation to Reduce Our Carbon Footprint

DYE-SENSITIZED AND PEROVSKITE SOLAR CELLS:
INTERFACE ENGINEERING BY ATOMIC LAYER DEPOSITION

INVERTED ORGANIC PHOTOVOLTAIC DEVICES
USING ZINC OXIDE NANOCOMPOSITES AS ELECTRON TRANSPORTING LAYER MATERIALS

KINETIC ENERGY HARVESTING
BY MAGNETOSTRICTIVE MATERIALS

LITHIUM-ION BATTERY PERFORMANCE:
DEPENDENCE ON MATERIAL SYNTHESIS AND POST-TREATMENT METHODS

SCALING UP HIGH-ENERGY CATHODE MATERIALS
FOR ELECTRIC VEHICLES

SIGMA-ALDRICH®

Introduction

Welcome to the fourth issue of *Material Matters™* for 2014, focusing on *Materials for Energy Harvesting and Storage*. Energy is vital for economic growth and, since the industrial revolution, carbon-based fossil fuels have served as the major energy source powering the growth of our economy and society. However, the ever-growing demand for energy has put tremendous pressure on conventional fossil energy resources, and it has become apparent that alternative renewable energy based on solar, wind, and hydrogen must cater to future needs. In order for alternative energy to become a viable contributor to the global energy supply, two challenges must be overcome.

Niraj K. Singh, Ph.D.
Aldrich Materials Science

First, the efficiency of the energy generation must increase to render it cost effective. Second is the development of high-performance storage devices, since the majority of alternative energy sources rely on sporadic power supplies. Solar energy represents the largest segment of non-carbon-based energy, and recently, significant effort has been put into harvesting solar power. Also, over the last few years, lithium-ion batteries (LIBs) have emerged as one of the most promising energy storage devices mainly due to their high energy density storage capacity. Some important challenges associated with energy harvesting device fabrication and storage are discussed in this issue.

In our first article, Prof. Mariadriana Creatore (Eindhoven University of Technology, Netherlands), discusses the benefits of fabricating meso-structured dye-sensitized and hybrid organometal perovskite solar cells using atomic layer deposition (ALD). In addition, the authors also elaborate on the use of ALD for deposition of Pt nanoparticles at the interface between the liquid electrolyte and a highly transparent counter electrode which improves the efficiency of charge transfer in a flexible DSC.

In the second article, Dr. Bryce Nelson (Aldrich Materials Science, USA), reviews recent developments in inverted bulk heterojunction organic photovoltaics. Particularly, progress in high efficiency inverted polymer solar cells using zinc oxide (ZnO) as electron-transporting layer (ETL) material and the new methods to improve surface and electronic properties of inverted OPVs that use ZnO are reviewed.

Prof. Daniele Davino (University of Sannio, Italy), in the third article, describes the macroscopic properties of magnetostrictive materials. Principals of kinetic energy harvesting using magnetostrictive materials along with relevant properties are also discussed.

In the fourth article, Prof. Guozhong Cao (University of Washington Seattle, USA) reviews the performance, such as capacity and cyclic stability, of several lithium-ion electrode materials. It has been shown that the performance of electrode materials heavily relies on composition, morphology, crystal structure, and defects.

For our fifth article, Gregory Krumdick (Argonne National Laboratory, USA) highlights the critical link between process development and scale-up of lithium-ion battery materials. The intricacies of the scale-up process and its effect on electrochemical properties are elaborated.

Each article in this publication is accompanied by a list of relevant materials available from Aldrich® Materials Science. For additional product information, visit us at aldrich.com/matsci. Send your comments or suggestions for *Material Matters* or your product suggestions to matsci@sial.com. We look forward to hearing from you.

About Our Cover

Development of advanced materials for both alternative energy generation and storage is critical for reducing our carbon footprint. The cover art of this issue shows examples of alternative energy generation and storage devices, emphasizing these new technologies will lead to a cleaner environment. We offer a large variety of innovative materials to help enable these alternative energy and storage technologies.

Table of Contents

Articles

Your Materials Matter

Bryce P. Nelson, Ph.D.
Aldrich Materials Science Initiative Lead

We welcome fresh product ideas. Do you have a material or compound you wish to see featured in the Aldrich® Materials Science line? If it is needed to accelerate your research, it matters. Send your suggestion to matsci@sial.com for consideration.

Prof. Dr. Christoph Brabec (Friedrich-Alexander-University Erlangen-Nuremberg, Germany) recommended the addition of ZnO nanoparticle dispersion in isopropanol (N-10, Aldrich Prod. No. 793361) to our catalog as an electron transport or electron injection material for organic electronics. N-10 exhibits superior printing and coating behavior at very low annealing temperatures of less than 100 °C. The resulting films are homogenous and show a very good electronic performance and enhanced lifetime. Significant potential lies in the suitability of N-10 for roll-to-roll processes with good wetting behavior and re-dissolution resistance. The figure below shows a printed layer of N-10 in a functioning organic photovoltaic cell. The electron transport layer N-10 is depicted in gold and is sandwiched between silver nanowires and the photoactive polymer layer.

Ag Nanowires
N-10, Aldrich Prod. No. 793361
Active Layer (DPP:PCBM)
PEDOT:PSS
ITO
300 nm
Glass Substrate
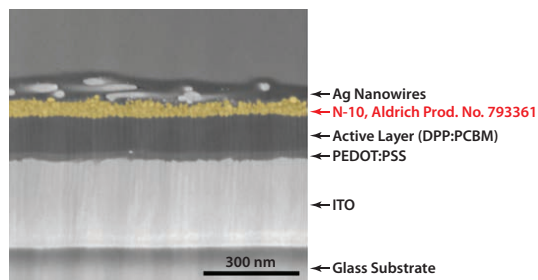
References

(1) Li, N.; Stubhan, T.; Krantz, J.; Machui, F.; Turbiez, M.; Ameri T.; Brabec, C.J. *J. Mater. Chem. A* **2014**, *2*, 14896–14902.
(2) Spyropoulos, G.D.; Kubis, P.; Li, N.; Baran, D.; Lucera, L.; Salvador, M.; Ameri, A.T.; Voigt, M.M.; Krebs, F.C.; Brabec, C.J. *Energy Environ. Sci.* **2014**, *7*, 3284–3290.
(3) Min, J.; Luponosov Y.N.; Zhang, Z.; Ponomarenko, S.A; Ameri, T.; Li, Y.; Brabec, C.J. *Adv. Energy Mater.* **2014**, 1400816.

Zinc oxide nanoparticle ink

ZnO
Nanograde N-10; ZnO ink; ZnO nanoparticle ink

793361-5ML	5 mL
793361-25ML	25 mL

DYE–SENSITIZED AND PEROVSKITE SOLAR CELLS:
INTERFACE ENGINEERING BY ATOMIC LAYER DEPOSITION

Valerio Zardetto,[1] Francesco Di Giacomo,[2] Thomas M. Brown,[2] Aldo Di Carlo,[2]
Alessandra D'Epifanio,[3] Silvia Licoccia,[3] Erwin Kessels,[1] Mariadriana Creatore[1*]
[1]Department of Applied Physics, Eindhoven University of Technology
P.O. Box 513, 5600 MB Eindhoven, The Netherlands
[2]Centre for Hybrid and Organic Solar Energy (CHOSE), Department of Electronic Engineering
University of Rome "Tor Vergata," via del Politecnico 1, 00133, Rome, Italy
[3]Department of Chemical Science and Technologies, University of Rome "Tor Vergata,"
Via della Ricerca Scientifica, 00133, Rome, Italy
*Email: M.Creatore@tue.nl

Introduction

Since the demonstration of the first practical solar cell 60 years ago, research on novel materials, improved solar cell design and structure, and innovative manufacturing processes have all contributed to a continuous increase in the efficiency of photovoltaic (PV) devices.[1] At a materials science level, fundamental studies primarily focus on the process of photocurrent generation, including charge carrier generation, charge transport and separation at the junction, and charge collection at the contacts. Equally important is the synthesis and development of highly absorbing thin active layers, as well as highly transparent and conductive contacts. The literature points out the importance of precisely engineering each interface of a PV structure at the nanoscale level in order to obtain higher power conversion efficiencies.[2,3] For instance, in crystalline silicon (c-Si) PV devices, ultra-thin oxides applied to the front and back surface of the wafer significantly reduce charge surface recombination processes either through chemical- or field-effect passivation.[2] Accurate control at the interface level is of the utmost importance for the most recent, low-cost PV technologies, such as organic photovoltaics (OPV), dye-sensitized solar cells (DSCs), and organometal halide perovskite solar cells, where nano- and meso-structured 3D interfaces are present. This additional understanding of the interface has contributed significantly to the recent increase in power conversion efficiency for both bulk heterojunction organic and polymer solar cells (BHJ-OPV) during the last years.[3] Here, control of the photoactive BHJ layer is based on a nano-scale interpenetrating network of an electron acceptor and a donor polymer. This network rules the exciton dissociation and the charge transfer processes, while the interface

between the BHJ and electrodes influences the charge extraction. The result is OPV performance approaching 10%,[3,4] or even in excess of 10% in a tandem configuration.[5]

Atomic layer deposition (ALD) is a technique widely utilized in the PV field to meet the demand for sub-nm control over film properties and thickness.[6] Ultra-thin Al_2O_3 layers have been successfully applied using ALD on the surface of crystalline silicon to form excellent passivation layers.[7] In copper indium gallium (di)-selenide (CIGS) solar cells, where the control of the interface between the absorber and the n-type window layer is essential, cadmium-free ALD buffer layers such as (Zn,Mg)O and Zn(O,S) have been developed to improve the band alignment with the CIGS absorber.[8] In this contribution, we first discuss the benefits of ALD when used for the fabrication of meso-structured DSCs and for hybrid organometal halide perovskite solar cells. In both architectures, the deposition of thin ALD metal oxides leads to an improvement in the device photo-voltage and current by suppressing selected interfacial charge recombination processes. In addition, we address the use of ALD for the deposition of Pt nanoparticles, which allows for efficient charge transfer at the interface between the liquid electrolyte and a highly transparent counter electrode (CE) in a flexible DSC.

Atomic Layer Deposition

ALD is a cyclic vapor phase deposition technique that enables the synthesis of thin films with atomic level control using sequential, self-limiting surface reactions (i.e., once all the active surface sites have reacted with the precursors, the reaction is completed). **Figure 1** representss an ALD process based on the repetition of two half cycles. Self-limited reactions occur between the surface and the precursor (first half cycle) and then the reactant (second half cycle). Purge steps are required to guarantee the absence of a chemical vapor deposition (CVD) contribution since they avoid the direct contact between the precursor and reactant. Therefore, the film thickness increases linearly as a function of the number of ALD cycles.
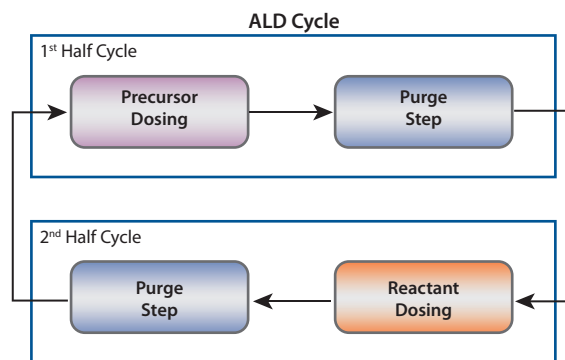
Figure 1. Schematic representation of an ALD cycle.

The reactant in the second half cycle can be water vapor, for example, for oxides. In this case, the reaction is driven by the temperature of the surface/substrate (Thermal ALD). Thermal ALD provides superior uniformity over large areas and excellent conformability in structures with a high aspect ratio, such as porous and nanostructured films. Plasma-assisted ALD is an alternative approach in which the reactant dose is replaced with a plasma exposure step. Plasma-assisted ALD offers several advantages compared to thermal processes, especially at low temperatures. The high reactivity of the plasma species (ions, metastables, and radicals) allows for: (1) the tuning of the chemical composition of the layer; (2) the development of higher density films (e.g., through an accurate control of the ion energy and flux); and (3) processing at lower temperatures, even down to room temperature,[9,10] making the process compatible with thermally sensitive substrates. One disadvantage of plasma-assisted ALD is reduced conformability, which particularly impacts the coating of complex 3D structures compared to other methods.[11]

Passivation Layers on Mesoscopic Structures

A conventional DSC (**Figure 2A**) is generally composed of a nanocrystalline TiO_2 mesoporous film deposited on a transparent conductive oxide (TCO) coated glass or polymer substrate. Dye molecules are adsorbed on the large TiO_2 surface area and act as light harvesters. A redox liquid electrolyte (e.g., I^-/I_3^-) and a counter electrode (Pt/TCO/substrate) complete the architecture.[12]
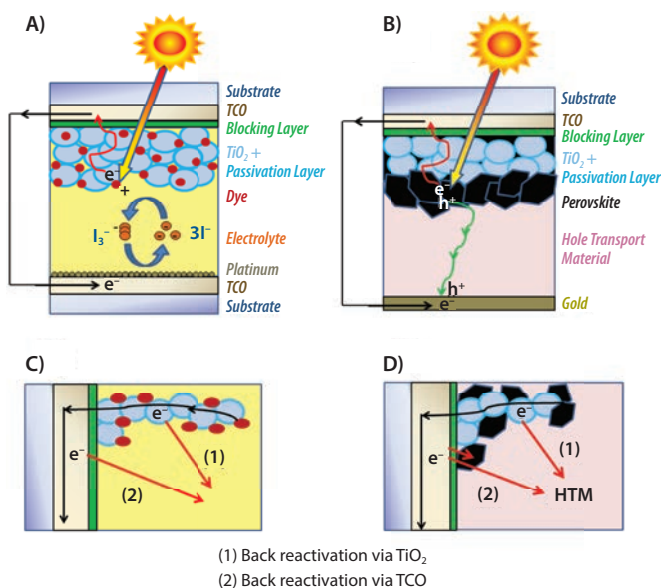
Figure 2. Configuration of hybrid mesoscopic solar cells: A) dye-sensitized and B) perovskite solar cells. The application of passivation and blocking layers has the purpose of limiting the primary interfacial back reactions in C) dye-sensitized and D) perovskite solar cells.

(1) Back reactivation via TiO_2
(2) Back reactivation via TCO

While the mesoporous structure is useful for efficient light harvesting, the huge internal surface area also increases recombination processes at the interface between the non-sensitized TiO_2 matrix and the liquid electrolyte. Here back charge transfer reactions occur between the electrons and the oxidized species (I_3^-),[13] as shown in **Figure 2C**. The

application of an ultra-thin dielectric layer, generally a wide band gap metal oxide (Al_2O_3, HfO_2, Ga_2O_3),[14–16] to form a high recombination energy barrier (**Figure 3A**) is a well-known strategy for reducing this recombination mechanism. In **Figure 3A**, thermal ALD was used to deposit an Al_2O_3 layer on TiO_2 nanoparticles (Aldrich Prod. No. 791326)—precise control of the oxide film thickness is essential to enable a sufficient passivation without reducing electron injection efficiency via tunnelling from the dye molecules to the TiO_2 conduction band.

The deposition of a single Al_2O_3 ALD cycle leads to the best results in terms of short circuit current (J_{SC}) and open circuit voltage (V_{OC}) and, consequently, in terms of power conversion efficiency (+17%) (**Figure 3B**). Increasing the Al_2O_3 thickness with the number of ALD cycles (over 5) reduces the short circuit current (J_{SC}), although an increment of the V_{OC} is also observed. The presence of the ultra-thin ALD layer influences the energy barrier height at the Al_2O_3/TiO_2 and Al_2O_3/dye interfaces, thereby controlling the recombination and the electron charge transfer processes, respectively.[17] A thicker Al_2O_3 layer is responsible for the reduction in tunnelling through the metal oxide and the suppression of the back reaction, therefore decreasing the J_{SC} value.
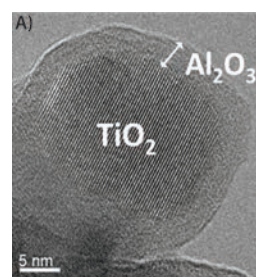
ALD Cycles	η (%)	J_{SC} (mA cm^{-2})	V_{OC} (mV)	FF (%)
0	4.35 ± 0.10	-10.15 ± 0.25	703 ± 8	62.4 ± 0.1
1	5.08 ± 0.06	-11.21 ± 0.31	725 ± 7	62.5 ± 1.5
5	4.55 ± 0.02	-10.50 ± 0.07	712 ± 2	60.4 ± 0.1
10	4.15 ± 0.08	-9.25 ± 0.06	728 ± 3	59.8 ± 0.1
20	2.62 ± 0.09	-5.41 ± 0.21	760 ± 5	66.0 ± 0.7

Figure 3. A) High-resolution TEM of thermal ALD Al_2O_3 on a nanocrystalline TiO_2 mesoporous film. B) Photovoltaic performance in terms of efficiency (η), short circuit current (J_{SC}), open circuit voltage (V_{OC}), and fill factor (FF) at 1 SUN of illumination for DSCs (active area of 0.25 cm^2) as a function of the number of ALD cycles.

Recently, replacement of the liquid electrolyte with a hole transport material (HTM) and breakthroughs using organolead halide perovskite as absorbers (generally $CH_3NH_3PbX_3$ with X=halogen) have led to the development of completely solid-state devices (**Figure 2B**) with efficiency values as high as 17.9%.[18] Although the ambipolar transport behavior of the perovskite also allows the fabrication of planar architectures similar to thin film PV devices, the application of a mesostructured TiO_2 scaffold has been found to lead to superior efficiency and stability.[19] In this architecture, the parasitic back reactions at the interface between the mesoporous TiO_2 film and the hole conductor stack perovskite/HTM are found to limit the V_{OC} of the device. An ultra-thin (2 nm) conformal ALD TiO_2 layer applied over the mesoscopic structure has been shown to also act as a passivation layer in high-efficiency perovskite solar cells.[20]

Blocking Layers on Transparent Conductive Oxides

A second recombination pathway in DSCs is at the interface between the TCO and the liquid electrolyte (**Figure 2C**), where the electrons can be captured by the oxidized species (I_3^-). In solid-state perovskite solar cells the interface TCO/hole conductor (both the perovskite and HTL layer) is characterized by a significant back transfer process affecting device performance (**Figure 2D**).[20–23] The current state-of-the art approach to reducing this recombination mechanism is the introduction of a blocking layer (BL) in both architectures. This layer must be extremely compact to exhibit rectifying behavior. ALD techniques are ideally suited for the delivery of such ultra-thin layers compared to other methodologies such as spray pyrolysis, sputtering, electrodeposition, and sol-gel.[22,23] For example, thermal ALD has been used already for the deposition of an ultra-thin (5–10 nm) TiO_2 compact layer on FTO/glass substrate for use in a DSC device.[24]

Plasma-assisted ALD allows the deposition of higher quality films on planar surfaces in a temperature range compatible with lightweight plastic substrates, which are suitable for low-cost manufacturing methods such as continuous roll-to-roll.[25] Plasma-assisted ALD processes have been adopted to deposit TiO_2 and ultra-thin Al_2O_3 and SiO_2 blocking layers at 150 °C on indium tin oxide (ITO)/PEN in DSC architecture.[26] The presence of a compact BL affects the cell performance depending on the level of illumination. Under full illumination (1 SUN), only a small variation in the generated power is discernible; whereas, under low level illumination, substantial improvements (Al_2O_3: +26%; SiO_2: +33%; and TiO_2: +40%) have been observed, as summarized in **Figure 4**.
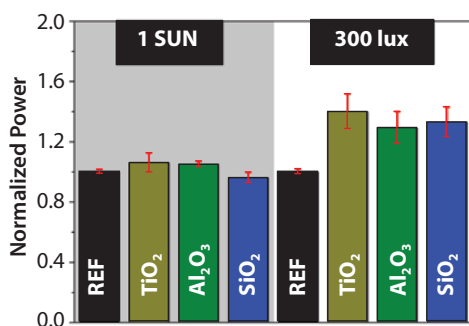
Figure 4. Normalized power of the DSCs using Al_2O_3 (four ALD cycles), SiO_2 (six ALD cycles), and TiO_2 (100 ALD cycles) blocking layers deposited by plasma-assisted ALD as compared to a reference cell (REF) without a blocking layer at different irradiations (1 SUN and indoor - 300 lux with CFL lamp).

Introduction of compact BLs is relevant for low light intensity conditions, where the photogenerated current is in the order of $\mu A \cdot cm^{-2}$ instead of $mA \cdot cm^{-2}$. This increase in the performance could be a crucial step for the exploitation of flexible DSCs for indoor applications and for their integration in portable electronics. In contrast, for high levels of illumination the slight variation is ascribed to the minor impact of the back charge transfer process at the ITO/electrolyte interface with respect to the photo-charge collection mechanism, as already observed in the presence of another TCO, fluorine tin oxide (FTO) used in glass-based devices.[27]

The electron recombination at the TCO/perovskite and hole conductor interfaces also has been recognized as a significant loss factor for perovskite solid-state devices. In particular, the back charge transfer process between the ITO surface and the hole conductor is important as

a recombination channel, when compared to the same process occurring at the interface of the ITO/electrolyte in plastic-based DSCs and the FTO/hole conductor interface in glass-based perovskite solar cells.[26,28] The absence of the blocking layer on an ITO/PET substrate is so detrimental that it has led to extremely low V_{OC} values (50 mV). The deposition of an 11 nm thick TiO_2 layer significantly decreases recombination and enables the fabrication of a flexible device with an efficiency of 7.4% (**Figure 5**).
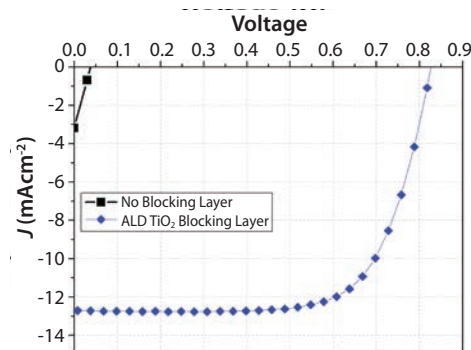
Figure 5. Photocurrent density–voltage curve for the mesoscopic perovskite solar cell with (and without) the TiO_2 blocking layer.

Platinum Nanoparticles on ITO/PEN Substrates

In the liquid-based DSC architecture, the interface between the platinum layer, generally composed of nanoparticles (NPs), and the electrolyte (**Figure 2A**) plays a key role in the charge transfer process for the reduction of the oxidized species I_3^- to $3I^-$. Recently, low-temperature processing by plasma-assisted ALD has been successfully applied for the synthesis of platinum NPs (Aldrich Prod. No. 685453),[29] also on ITO/PEN substrates[30] (**Figure 6**). It has been found that the electro-catalytic properties of the counter-electrode are not only governed by the Pt loading but also by the NPs surface active area.[30] At the same time, a limited Pt loading is required to guarantee a highly transparent electrode for efficient light harvesting in the case of back-illuminated flexible DSCs.
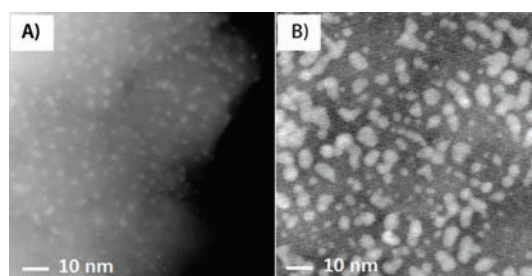
Figure 6. High-resolution TEM images of the platinum NPs prepared with 50 and 100 ALD cycles at 100 °C on ITO/PEN substrates.

Optimal cell power efficiency was achieved using 100 ALD cycles, corresponding to a Pt loading of 390 $nm \cdot cm^{-2}$ with an average particle size of 3 nm and a transparency of 95%. Furthermore, when compared to conventional methods (sputtering and electrodeposition) adopted in literature for ITO-polymer substrates, ALD-prepared NPs exhibit equivalent electro-catalytic activity properties but higher transparency (+10%), leading to an improved solar cell efficiency (+19%).[30]

Summary

Precise engineering and a high degree of control at the interfaces within a solar cell are vital for the improvement of its performance. The application of ALD to the latest generation of solar cells, such as dye-sensitized and perovskite, has been addressed here. Both thermal and plasma-assisted ALD approaches have been successfully adopted to fabricate dielectric and semiconductor ultra-thin films and metal nanoparticles on different substrates. ALD Al_2O_3 passivation layers on mesoporous structures and different compact blocking layers on TCOs suppress the charge recombination processes at complex interfaces within the device. Furthermore, control over the loading and size of Pt NPs on PEN/ITO substrates allows for a compromise between the charge transfer properties of the counter-electrode and its optical transparency for back-side illuminated DSCs. All these applications demonstrate how ALD can be a successful approach for achieving nanoscale control in mesoscopic solar cells.

Acknowledgments

References

(1) Green, M.A.; Emery, K.; Hishikawa, Y.; Warta, W.; Dunlop, E.D. *Prog. Photovoltaics Res. Appl.* **2014**, *22*, 701.
(2) Green, M.A., Zhao, J.; Wang, A.; Wenham, S.R. *IEEE Trans. Electron Dev.* **1999**, *46*, 1940.
(3) Graetzel, M.; Janssen, R.A.J.; Mitzi, D.B.; Sargent, E.H. *Nature* **2012**, *488*, 304.
(4) Chen, S.; Manders, J.R.; Tsang, S.W.; So, F. *J. Mater. Chem.* **2012**, *22*, 24202.
(5) You, J.; Dou, L.; Yoshimura, K.; Kato, T.; Ohya, K.; Moriarty, T.; Emery, K.; Chen, C.C.; Gao, J.; Li, G.; Yang, Y. *Nature Commun.* **2013**, *4*, 1.
(6) van Delft, J.A.; Garcia-Alonso, D.; Kessels, W.M.M. *Semicond. Sci. Technol.* **2012**, *27*, 074002.
(7) Dingemans, G.; Kessels, W.M.M. *J. Vac. Sci. Technol. A* **2012**, *30*, 040802.
(8) Naghavi, N.; Abou-Ras, D.; Allsop, N.; Barreau, N.; Bücheler, S.; Ennaoui, A.; Fischer, C.-H.; Guillen, C.; Hariskos, D.; Herrero, J.; Klenk, R.; Kushiya, K.; Lincot, D.; Menner, R.; Nakada, T.; Platzer-Björkman, C.; Spiering, S.; Tiwari, A.N.; Törndahl, T. *Prog. Photovoltaics Res. Appl.* **2003**, *11*, 437.
(9) Potts, S.E.; Van den Elzen, L.R.; Dingemans, G.; Langereis, E.; Keuning, W.; Van de Sanden, M.C.M.; Kessels, W.M.M. *ECS Trans.* **2009**, *157*, 233.
(10) Kessels, W.M.M.; Heil, S.B.S.; Langereis, E.; van Hemmen, J.L.; Knoops, H.C.M.; Keuning, W.; van de Sanden, M.C.M. *ECS Transactions* **2007**, *3*, 183.
(11) Knoops, H.C.M.; Langereis, E.; van de Sanden, M. C. M.; Kessels, W.M.M. *J. Electrochem. Soc.* **2011**, *158*, G88.
(12) Grätzel, M., *J. Photochem. Photobiol. C*, **2003**, *4*, 145.
(13) Bisquert, J.; Fabregat-Santiago, F.; Mora-Sero, I.; Garcia-Belmonte, G.; Gimenez, S. *J. Phys. Chem. C* **2009**, *113*, 17278.
(14) Shanmugam, M.; Baroughi, M.F.; Galipeau, D. *Thin Solid Films* **2010**, *518*, 2678.
(15) Chandiran, A.K.; Tetreault, N.; Humphry-Baker, R.; Kessler, F.; Baranoff, E.; Yi, C.; Nazeeruddin, M.K.; Grätzel, M. *Nano Lett.* **2012**, *12*, 3941.
(16) Liberatore, M.; Burtone, L.; Brown, T.M.; Reale, A.; Di Carlo, A.; Decker, F.; Caramori, F.; Bignozzi, C.A. *Appl. Phys. Lett.* **2009**, *94*, 173113.
(17) Tien, T.C.; Pan, F.M.; Wang, L.P.; Lee, C.H.; Tung, Y.L.; Tsai, S.Y.; Lin, C.; Tsai, F.Y.; Chen, S.J. *Nanotechnology* **2009**, *20* 305201.
(18) Green, M.A.; Ho-Baillie, A.; Snaith, H.J. *Nature Photonics* **2014**, *8*, 506.
(19) Gao, P.; Nazeeruddin, M.K.; Grätzel, M. *Energy Environ. Sci.* **2014**, *7*, 2448.
(20) Chandiran, A.K.; Yella, A.; Mayer, M.T.; Gao, P.; Nazeeruddin, M.K.; Grätzel, M. *Adv. Mater* **2014**, *26*, 4309.
(21) Juarez-Perez, E.J.; Wußler, M.; Fabregat-Santiago, F.; Lakus-Wollny, K.; Mankel, E.; Mayer, T.; Jaegermann, W.; Mora-Sero, I. *J. Phys. Chem. Lett.* **2014**, *5*, 680.
(22) Kavan, L.; Tétreault, N.; Moehl, T.; Grätzel, M.; *J. Phys. Chem.*, **2014**, DOI: 10.1021/jp4103614.
(23) Wu, Y.; Yang, X.; Chen, H.; Zhang, K.; Qin C.; Liu, J.; Peng, W.; Islam, A.; Bi, E.; Ye, F. *Appl. Phys. Express* **2014**, *7*, 052301.
(24) Kim, D.H.; Woodroof, M.; Lee, K.; Parsons, G.N. *ChemSusChem* **2013**, *6*, 1014.
(25) Brown, T.M.; De Rossi, F.; Di Giacomo, F.; Mincuzzi, G.; Zardetto, V.; Reale, A.; Di Carlo, A. *J. Mater. Chem. A* **2014**, *2*, 10788.
(26) Zardetto, V.; Di Giacomo, F.; Garcia-Alonso, D.; Brown, T.M.; Di Carlo, A.; D'Epifanio, A.; Licoccia, S.; Kessels, W.M.M.; Creatore, M. *to be published*.
(27) Cameron, P.J.; Peter, L.M. *J. Phys. Chem. B* **2003**, *107*, 14394.
(28) Di Giacomo, F.; Zardetto, V.; D'Epifanio, A.; Matteocci, F.; Razza, S.; Di Carlo, A.; Kessels, W.M.M.; Creatore, M.; Licoccia, S.; Brown, T.M.; *submitted*.
(29) Mackus, A.J.M.; Garcia-Alonso, D.; Knoops, H.C.M.; Bol, A.A.; Kessels, W.M.M. *Chem. Mater.* **2013**, *25*, 1769.
(30) Garcia-Alonso, D.; Zardetto, V.; Mackus, A.J.M.; De Rossi, F.; Verheijen, M.A.; Brown, T.M.; Kessels, W.M.M.; Creatore, M. *Adv. Energy. Mater.* **2014**, *4*, 1300831.

CVD/ALD Precursors Packaged in Cylinders for Deposition Systems

For a complete list of CVD/ALD precursors packaged in cylinders for deposition systems, visit aldrich.com/ald.

Name	Acronym	Structure	Form	Prod. No.
Diethylzinc	DEZ; DEZn; Et₂Zn	H_3C—Zn—CH_3	liquid	668729-25G
Tetrakis(diethylamido)titanium(IV)	TDEAT	(structure)	liquid	725536-10G
Tetrakis(dimethylamido)titanium(IV)	TDMAT	(structure)	liquid	669008-25G
Tetrakis(dimethylamido)zirconium(IV)	TDMAZ	(structure)	solid	669016-25G

Name	Acronym	Structure	Form	Prod. No.
Tetrakis(ethylmethylamido)zirconium(IV)	TEMAZ		liquid	725528-10G
Titanium(IV) isopropoxide	TTIP		liquid	687502-25G
Titanium tetrachloride	TTC	$TiCl_4$	liquid	697079-25G
Triethylgallium	TEG; TEGa; Et₃Ga		liquid	730726-10G
Trimethylaluminum	TMA		liquid	663301-25G
Trimethylgallium	TMG; TMGa; Me₃Ga		liquid	730734-10G
Trimethyl(methylcyclopentadienyl)platinum(IV)	MeCpPtMe₃		low-melting solid	697540-10G
Water	-	H_2O	liquid	697125-25ML
Zirconium(IV) tert-butoxide	ZTB		liquid	759554-25G

Vapor and Solution Deposition Precursors for Energy Applications

For a complete list of vapor and solution deposition precursors for energy applications, visit aldrich.com/mnel.

Name	Structure	Purity	Form	Prod. No.
Copper bis(6,6,7,7,8,8,8-heptafluoro-2,2-dimethyl-3,5-octanedionate)		≥99.99% trace metals basis	solid	541761-1G 541761-5G
Copper bis(2,2,6,6-tetramethyl-3,5-heptanedionate)		99%	solid	345083-1G
Gallium(III) acetylacetonate		99.99% trace metals basis	solid	393541-5G 393541-25G
Indium(III) acetate hydrate		99.99% trace metals basis	powder and chunks	342378-5G 342378-25G
Indium(III) acetylacetonate		≥99.99% trace metals basis	solid	I3300-5G
Tetrakis(dimethylamido)titanium(IV)		99.999% trace metals basis	liquid	469858-5G 469858-25G
Tetrakis(dimethylamido)zirconium(IV)		≥99.99% trace metals basis	solid	579211-5G
Trimethylaluminum		97%	liquid	257222-100G

Name	Structure	Purity	Form	Prod. No.
Tris(dimethylamido)gallium(III)		98%	solid	546534-5G
Yttrium(III) acetylacetonate hydrate		99.95% trace metals basis	powder or crystals	438790-5G
Yttrium 2-methoxyethoxide solution		~5 wt. % Y basis	liquid	771538-25G
Zirconium(IV) tert-butoxide		99.999% trace metals basis	liquid	560030-5G
560030-25G
Zirconium(IV) 2-ethylhexanoate in mineral spirits		~6% Zr basis	liquid	768634-50G
Zirconium tetrakis(2,2,6,6-tetramethyl-3,5-heptanedionate)		≥99.99%	solid	478865-5G
478865-25G

Sputtering Targets

For a complete list of sputtering targets for energy applications, visit aldrich.com/pvd.

Name	Composition	Dimensions (in.)	Purity	Prod. No.
Aluminum	Al	3.00 × 0.125	99.9995% trace metals basis	749036-1EA
Chromium	Cr	3.00 × 0.125	99.95% trace metals basis	749052-1EA
Indium tin oxide	In_2O_3 / SnO_2	3.00 × 0.125	99.99% trace metals basis	752657-1EA
Zinc	Zn	3.00 × 0.125	99.995% trace metals basis	749060-1EA
Zinc oxide	ZnO	3.00 × 0.125	99.99% trace metals basis	752681-1EA

Substrates for Thin Film Deposition

For a complete list of substrates for thin film deposition, visit aldrich.com/substrates.

Name	Composition	Dimensions	Orientation	Prod. No.
Aluminum oxide	Al_2O_3	L × W × thickness 10 × 10 × 0.5 mm	<0001>	634875-1EA
634875-5EA
Magnesium aluminate	$MgO·Al_2O_3$	L × W × thickness 10 × 10 × 0.5 mm	<100>	635073-1EA
Magnesium oxide	MgO	L × W × thickness 10 × 10 × 0.5 mm	<100>	634646-1EA
Silicon	Si	diam. × thickness 2 in. × 0.5 mm	<100>	646687-1EA
646687-5EA
	Si	diam. × thickness 3 in. × 0.5 mm	<100>	647535-1EA
647535-5EA
	Si	diam. × thickness 2 in. × 0.5 mm	<111>	647101-1EA
647101-5EA
Silicon dioxide	SiO_2	L × W × thickness 10 × 10 × 0.5 mm	<0001>	634867-5EA

ALDRICH®
Materials Science

CADMIUM-FREE
QUANTUM DOTS

Quantum dots exhibit excellent photoluminescence and electroluminescence properties such as narrow emission bandwidth and high brightness. The toxicity of cadmium makes Cd-free quantum dots more desirable for consumer applications.

Use Cd-free Quantum Dots for these applications:

- LEDs
- Displays
- Solid-state lighting
- Photovoltaics
- Transistors, etc.

Name	Description	Fluorescence Emission (λ_{em})	Prod. No.
InP/ZnS Core-Shell Type Quantum Dots	Kit, 5 × 5 mg/mL in toluene, stabilized with oleylamine ligands	530–650 nm	777285
	5 mg/mL in toluene, stabilized with oleylamine ligands	530 nm	776750
	5 mg/mL in toluene, stabilized with oleylamine ligands	560 nm	776793
	5 mg/mL in toluene, stabilized with oleylamine ligands	590 nm	776769
	5 mg/mL in toluene, stabilized with oleylamine ligands	620 nm	776777
	5 mg/mL in toluene, stabilized with oleylamine ligands	650 nm	776785
PbS Core-type Quantum Dots	Kit, 4 × 10 mg/mL in toluene, oleic acid coated	1,000–1,600 nm	790494
	10 mg/mL in toluene, oleic acid coated	1,000 nm	747017
	10 mg/mL in toluene, oleic acid coated	1,200 nm	747025
	10 mg/mL in toluene, oleic acid coated	1,400 nm	747076
	10 mg/mL in toluene, oleic acid coated	1,600 nm	747084

Learn more about quantum dot properties and applications, including our complete product offering, at
aldrich.com/quantumdots

SIGMA-ALDRICH®

INVERTED ORGANIC PHOTOVOLTAIC DEVICES
USING ZINC OXIDE NANOCOMPOSITES AS ELECTRON TRANSPORTING LAYER MATERIALS
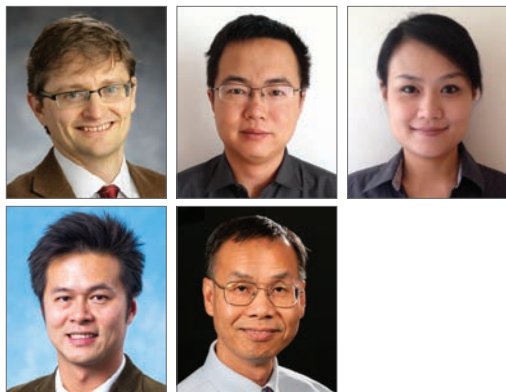
Bryce P. Nelson,[1]* Pengjie Shi,[1] Wei Wei,[1] Sai-Wing Tsang[2] and Franky So[3]
[1]Aldrich Materials Science, Sigma-Aldrich Co. LLC
6000 N. Teutonia Ave., Milwaukee, WI, USA 53209
[2]Sai-Wing Tsang, Department of Physics and Materials Science
City University of Hong Kong, Hong Kong SAR, China
[3]Department of Materials Science and Engineering, University of Florida, Gainesville, FL, USA
*Email: Bryce.nelson@sial.com

Introduction

Organic photovoltaics (OPVs) represent a low-cost, lightweight, and scalable alternative to conventional solar cells. While significant progress has been made in the development of conventional bulk heterojunction cells, new approaches are required to achieve the performance and stability necessary to enable commercially successful OPVs. Inverted bulk heterojunction OPVs are one promising approach. This review highlights recent progress in high efficiency inverted polymer solar cells using zinc oxide (ZnO) as an electron-transporting layer (ETL) material, as well as new methods to improve surface and electronic properties of inverted OPVs that use ZnO.

Recent research efforts in the OPV field have largely focused on the development of novel photoactive polymers or small organic molecules for use in conventional bulk heterojunction cells. These efforts have led to power conversion efficiencies (PCEs) of up to 7–8%. In a conventional OPV cell configuration, the anode layer typically consists of a thin layer of indium tin oxide (ITO) coated with a p-type interface layer of poly(3,4-ethylenedioxythiophene):poly(styrene sulfonate) (PEDOT:PSS). ITO is frequently used because it is conductive, transparent, and has a high work function. As a hole transporting layer, PEDOT:PSS fills pinholes in the ITO film and forms Ohmic contact with the photoactive layer. The cathode layer in a conventional OPV is typically constructed from low-work function metals such as calcium, aluminum, and magnesium. Since low-work function materials are easily oxidized when exposed to air, the cathodes must be encapsulated to prevent exposure. While some researchers have worked to develop cathodes using less reactive materials, this approach can add expense, impact performance, and/or add complexity to the OPV.

The inverted OPV configuration reverses the conventional OPV layer sequence to avoid the use of easily oxidized metals on the exposed cathode, improve device stability, and improve overall device performance. **Figure 1A** shows a diagram of an inverted OPV. A layer of a low-work function material is positioned directly on top of the ITO electrode to form the ETL, thus converting it to a cathode. Typical ETL materials used in inverted OPVs include cesium carbonate (Cs_2CO_3), n-type metal oxides such as titanium oxide (TiO_x) and zinc oxide (ZnO), as well as alcohol or water-soluble conjugated polyelectrolytes. The anode interlayer, or hole transporting layer, is most often fabricated from poly(3,4-ethylenedioxythiophene):poly(styrene sulfonate) (PEDOT:PSS) or one of many high-work function transition metal oxides including MoO_3, WO_3, and V_2O_5.[4] Silver (Ag) is widely used as the exposed layer in inverted OPVs because it forms an air-stable anode and can be applied using low cost coating and printing techniques. Many materials used in inverted OPVs can be processed in solution, greatly improving prospects for future manufacturing.
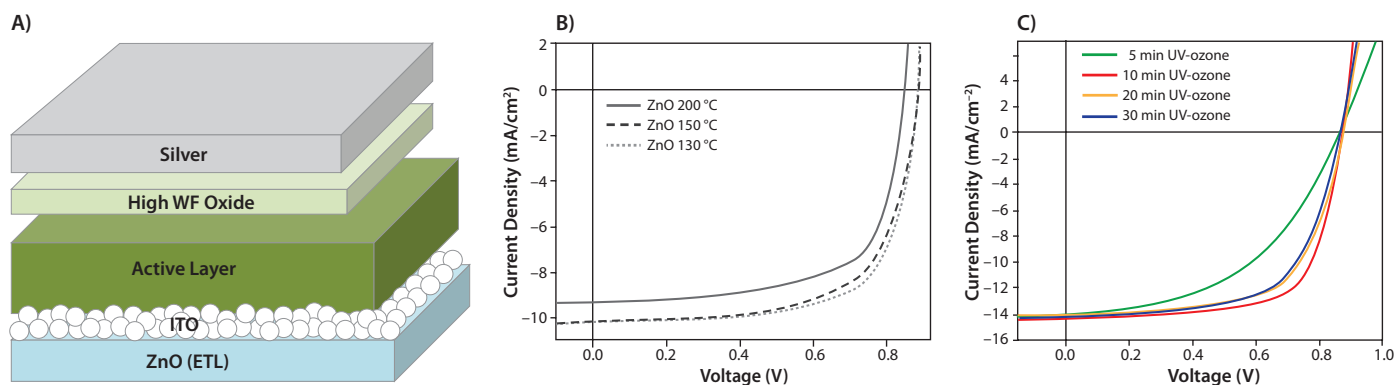
Figure 1. A) The device structure of a typical inverted polymer solar cell. **B)** J-V characteristics of inverted PCDTBT:PC$_{70}$BM solar cells incorporating ZnO films with the indicated annealing temperatures. Adapted from Reference 13. Copyright 2011 Wiley-VCH Verlag GmbH & Co. KGaA. **C)** J-V characteristics of inverted PDTG–TPD:PC$_{70}$BM solar cells with different UVO treatment time of ZnO-PVP ETL under 100 mWcm^{-2} AM 1.5 G illumination. Adapted from Reference 17. Copyright 2011 Macmillan Publishers Limited.

Low-temperature Annealed Sol-gel Derived ZnO Film as Electron Transport Layers

ZnO has shown particular promise as a cathode material for use in inverted OPV cells because of its relatively high electron mobility, stability, and transparency. In addition, ZnO thin films can be easily fabricated using highly scalable sol-gel application methods. One drawback of sol-gel methods in OPVs is the high annealing temperatures required to remove residual organic compounds and to promote oxide crystallization, which can be incompatible with polymers used in OPVs. To address this, Heeger et al.[13] tested low-temperature annealing to create sol-gel derived ZnO films in OPV cells. **Figure 1B** shows the *J-V* characteristics of inverted solar cells based on poly[N-9″-hepta-decanyl-2,7-carbazole-alt-5,5-(4′,7′-di-2-thienyl-2′,1′,3′-benzothiadiazole)] (PCDTBT, Aldrich Prod. No. 753998) and [6,6]-phenyl C_{70}-butyric acid methyl ester (PC$_{70}$BM, Aldrich Prod. No. 684465) that incorporate ZnO films annealed at different temperatures. These composites achieved a PCE of 6.33%. To fabricate these ZnO films, Heeger et al. applied zinc acetate in 2-methoxyethanol by spin-casting onto ITO substrates followed by thermal annealing to produce dense ZnO film by hydrolysis. While as-prepared sol-gel derived ZnO thin films are known to commonly be oxygen deficient, X-ray photoelectron spectroscopy (XPS) data from these ZnO films showed an increase of Zn-O bonds with increasing annealing temperature and thus a decrease in defect density. Additionally, the electron mobilities increased from 2.0×10^{-4} to 4.0×10^{-3} cm^2 V^{-1} s^{-1} upon annealing at 200 °C. Along with high PCE, the inverted cell showed improved device stability, with stable PCE performance after exposure to air for more than 30 days. A comparable conventional cell showed a PCE drop of more than 30% after 16 hr of air exposure.

UV-ozone Treated ZnO Nanocomposites as Electron Transporting Layers

ZnO-colloidal nanoparticles have been widely used in the development of inverted OPVs due to their ease of synthesis via hydrothermal methods. However, when ZnO nanoparticles are used as the ETL in inverted OPVs, the high density of defects of the as-synthesized nanoparticles results in lower fill factors compared to conventional devices. Recent work from the So group at the University of Florida has demonstrated the performance of inverted OPVs can be improved using UV-ozone (UVO) treatment of the ZnO nanoparticles. Steady-state photoluminescence (PL) measurement of ZnO thin film showed a broad emission peaked at 519 nm, with intensity comparable to the band-to-band emission at 372 nm, indicating defects in the ZnO nanoparticles. It has been shown the defects are mainly induced by oxygen adsorption on the ZnO nanoparticle surface and such defects can be reduced significantly by UVO treatment. The reduction of defects after the UVO treatment was confirmed by large suppression of the trap emission in the ZnO thin film and prolonged carrier lifetime in OPVs. As a result, the OPVs using UVO-treated ZnO as the ETL show significant improvement in short-circuit current (J_{SC}), suggesting the UVO treatment passivates the ZnO surface.

So et al. also developed a ZnO-poly(vinyl pyrrolidone) (PVP) nanocomposite for use as the ETLs in an inverted dithienogermole-thienopyrrolodione (PDTG-TPD)-based polymer solar cell. Here, the ZnO-PVP nanocomposite replaces ZnO colloidal nanoparticles for

modifying the work function of the ITO and enhancing its coupling to the active layer. Sol-gel derived ZnO-PVP nanocomposites have a number of advantages over ZnO-colloidal nanoparticles. For example, the PVP polymer passivates the ZnO surface, resulting in better stability. This passivation simplifies fabrication of the ETL device, enabling assembly in air. Second, the size and concentration of ZnO nanoclusters can be tuned by controlling the Zn^{2+}/PVP ratio. Third, the use of PVP reduces aggregation of ZnO nanoclusters, enabling more uniform thin films. Last, PVP passivates the ZnO nanoclusters and prevents oxygen from out-diffusion and the formation of defect states, as commonly found in inorganic–organic composite thin films.

However, one drawback of the ZnO-PVP nanocomposite is the presence of PVP hinders the coupling between ZnO and the photoactive layer. As a result, devices fabricated using unmodified ZnO-PVP typically perform poorly. By treating the composite film with UVO, the coupling between ZnO and the active layer is significantly enhanced and performance improves substantially. Surface analysis of UVO-treated films reveal the PVP polymer on the film surface is effectively removed by the UVO treatment, exposing ZnO on the surface. As a result, the electronic coupling between ZnO and the active layer is enhanced, allowing more efficient charge collection in the photovoltaic device. As shown in **Figure 1C**, such an improvement is directly reflected on the improvement of device fill factors, which increases from below 50% to 68%. Using this ZnO composite film, inverted OPVs with PCEs over 8% can be achieved with the low bandgap polymer PDTG-TPD.

Conclusion

Despite the potential advantages of high-performance inverted OPVs, comparatively few studies have focused on their development. Significant progress has been achieved in developing inverted polymer solar cells using zinc oxide nanocomposites as electron transporting layer materials. Although there are remaining questions on how to convert the small scale lab process into the massive production of flexible solar cell films, this research opens a bright future for efficient, light weight, and low-cost OPV devices.

References
(1) Wu, Y.; Li, Z.; Ma, W.; Huang, Y.; Huo, L.; Guo, X.; Zhang, M.; Ade, H.; Hou, J. *Adv. Mater.* **2013**, *25*, 3449.
(2) Dou, L.; Chen, C.-C; Yoshimura, K.; Ohya, K.; Chang, W.-H.; Gao, J.; Liu, Y.; Richard, E.; Yang, Y. *Macromolecules* **2013**, *46*, 3384.
(3) Nikiforov, M.P.; Strzalka, J.; Jiang, Z.; Darling, S.B. *Phys. Chem. Chem. Phys.* **2013**, *15*, 13052.
(4) Hau, S.K.; Yip, H.-L.; Jen, A.K.-Y. *Polymer Reviews* **2010**, *50*, 474.
(5) Liao, H.-H.; Chen, L.-M.; Xu, Z.; Li, G.; Yang, Y. *Appl. Phys. Lett.* **2008**, *92*, 173303.
(6) Park, S.H.; Roy, A.; Beaupre, S.; Cho, S.; Coates, N.; Moon, J.S.; Moses, D.; Leclerc, M.; Lee, K.; Heeger, A.J. *Nat. Photonics* **2009**, *3*, 297.
(7) White, M.S.; Olson, D.C.; Shaheen, S.E.; Kopidakis, N.; Ginley, D.S. *Appl. Phys. Lett.* **2006**, *89*, 143517.
(8) Norrman, K.; Madsen, M.V.; Gevorgyan, S.A.; Krebs, F.C. *J. Am. Chem. Soc.* **2010**, *132*, 16883.
(9) He, Z.; Zhong, C.; Su, S.; Xu, M.; Wu, H.; Cao, Y. *Nat. Photonics* **2012**, *6*, 591.
(10) Chen, S.; Manders, J.R.; Tsang, S.-W.; So, F. *J. Mater. Chem.* **2012**, *22*, 24202.
(11) Hau, S.K.; Yip, H.-L.; Leong, K.; Jen, A.K.-Y. *Org. Electron.* **2009**, *10*, 719.
(12) Cho, K.H.; Kang, M.G.; Oh, S.-M.; Kang, C.-Y.; Lee, Y.P.; Yoon, S.-J. *Thin Solid Films* **2010**, *518*, 6277.
(13) Sun, Y.; Seo, J.H.; Takacs, C.J.; Seifter, J.; Heeger, A.J. *Adv. Mater.* **2011**, *23*, 1679.
(14) Klenk, R. *Thin Solid Films* **2001**, *387*, 135.
(15) Chen, S.; Small, C.E.; Amb, C.M.; Subbiah, J.; Lai, T.H.; Tsang, S.W.; Reynolds, J.R.; So, F. *Adv. Energy Mater.* **2012**, *2*, 1333.
(16) Hartel, M.; Chen, S.; Swerdlow, B.; Hsu, H.-Y.; Manders, J.; Schanze, K.S.; So, F. *ACS Appl. Mater. Interfaces* **2013**, *5*, 7215.
(17) Small, C.E.; Chen, S.; Subbiah, J.; Amb, C.M.; Tsang, S.W.; Lai, T.H.; Reynolds, J.R.; So, F. *Nature Photon.* **2012**, *6*, 115.

Nanomaterials for Photovoltaics

For a complete list of available materials, visit aldrich.com/nanomaterials.

Titanium

Name	Size	Description	Form	Prod. No.
Titania paste, active opaque	avg. part. size 20 nm (active) avg. part. size ≤450 nm (scatter)	Crystal Structure: >99% Anatase (Analysis carried out on starting material; prior to paste manufacture)	paste (cream)	791555-5G 791555-20G
Titania paste, reflector	avg. part. size 150 - 250 nm (scatter)	Crystal Structure: >99% Anatase (Analysis carried out on starting material; prior to paste manufacture)	paste (white)	791539-5G 791539-20G
Titania paste, transparent	avg. part. size 20 nm (active)	Crystal Structure: >99% Anatase (Analysis carried out on starting material; prior to paste manufacture)	paste (yellow)	791547-10G 791547-20G
Titanium	particle size <100 nm	98.5% trace metals basis	dispersion nanoparticles	513415-5G
Titanium(IV) oxide	particle size 21 nm (TEM)	≥99.5% trace metals basis	nanopowder	718467-100G
Titanium(IV) oxide, anatase	particle size <25 nm	99.7% trace metals basis	nanopowder	637254-50G 637254-100G 637254-500G
Titanium(IV) oxide, mixture of rutile and anatase	particle size <100 nm (BET) particle size <50 nm (XRD)	99.5% trace metals basis	nanopowder	634662-25G 634662-100G
	particle size <250 nm (DLS) particle size ~21 nm (primary particle size of starting nanopowder)	99.9% trace metals basis	nanoparticles paste	700355-25G
	particle size ~21 nm (primary particle size of starting nanopowder) particle size <150 nm (volume distribution, DLS)	99.5% trace metals basis	dispersion nanoparticles	700347-25G 700347-100G
	particle size ~15 nm (primary particle size of starting nanopowder) particle size <100 nm (DLS)	99.9% trace metals basis	dispersion nanoparticles	700339-100G
Titanium(IV) oxide, rutile	particle size <100 nm, diam. × L ~10 × ~40 nm	99.5% trace metals basis	nanopowder	637262-25G 637262-100G 637262-500G

Zinc

Name	Size	Description	Form	Prod. No.
Zinc iron oxide	particle size <100 nm (BET)	>99% trace metals basis	nanopowder	633844-10G
Zinc oxide	particle size <100 nm	~80% Zn basis	nanopowder	544906-10G 544906-50G
	particle size <50 nm (BET)	>97%	nanopowder	677450-5G
	diam. × L 90 nm × 1 μm	-	nanowires	773999-500MG
	diam. × L 50 × 300 nm	-	nanowires	773980-500MG
	diam. × L 300 nm × 4-5 μm	-	nanowires	774006-500MG
Zinc oxide, dispersion	avg. part. size <35 nm (APS) particle size <100 nm (DLS)	50 wt. % in H$_2$O	nanoparticles	721077-100G
	avg. part. size <35 nm (APS) particle size <130 nm (DLS)	40 wt. % in ethanol	nanoparticles	721085-100G
	avg. part. size <35 nm (APS) particle size <110 nm (DLS)	40 wt. % in butyl acetate	nanoparticles	721093-100G
	avg. part. size <35 nm (APS) particle size <120 nm (DLS)	40 wt. % in butyl glycol	nanoparticles	721107-100G

Indium Tin Oxide (ITO) Coated Substrates

For a complete list of available ITO-coated substrates, visit aldrich.com/ito.

Name	L × W × Thickness (mm)	Surface Resistivity (Ω/sq)	Prod. No.
Indium tin oxide coated glass slide, rectangular	75 × 25 × 1.1	8-12	578274-10PAK 578274-25PAK
	75 × 25 × 1.1	15-25	636916-10PAK 636916-25PAK
	75 × 25 × 1.1	30-60	636908-10PAK 636908-25PAK
	75 × 25 × 1.1	70-100	576352-10PAK 576352-25PAK
Indium tin oxide coated glass slide, square	25 × 25 × 1.1	8-12	703192-10PAK
	25 × 25 × 1.1	70-100	703176-10PAK
	25 × 25 × 1.1	30-60	703184-10PAK
Indium tin oxide coated PET	1 ft × 1 ft × 5 mil	60	639303-1EA 639303-5EA
	1 ft × 1 ft × 5 mil	100	639281-1EA 639281-5EA
	1 ft × 1 ft × 5 mil	200	749745-1EA 749745-5EA
	1 ft × 1 ft × 5 mil	300	749796-1EA 749796-5EA
	1 ft × 1 ft × 5 mil	250	749761-1EA 749761-5EA

Fluorine-doped Tin Oxide (FTO) Coated Substrates

For a complete list of available FTO-coated substrates, visit aldrich.com/fto.

Name	L × W × D (mm)	Surface Resistivity (Ω/sq)	Prod. No.
Fluorine doped tin oxide coated glass slide	50 × 50 × 2.2	~7	735140-5EA
	100 × 100 × 2.3	~7	735159-5EA
	300 × 300 × 2	~7	735167-1EA
	50 × 50 × 2.2	~13	735248-5EA
	100 × 100 × 2	~13	735256-5EA
	300 × 300 × 2.3	~13	735264-1EA

PEDOT:PSS

For a complete list of available materials, visit aldrich.com/polythio.

Name	Sheet Resistance	Viscosity (cP)	pH	Prod. No.
dry re-dispersible pellets	resistance 200-450 Ω/sq	-	-	768618-1G 768618-5G
0.8% in H$_2$O, conductive inkjet ink	-	7-12 at 22 °C	1.5 - 2.5	739316-25G
1.1% in H$_2$O, neutral pH, high-conductivity grade	resistance <100 Ω/sq (>70% visible light transmission, 40 μm wet)	<100 at 22 °C	5 - 7	739324-100G
1.1% in H$_2$O, surfactant-free, high-conductivity grade	resistance <100 Ω/sq (<80% visible light transmission, 40 μm wet)	<100 at 22 °C	<2.5	739332-100G
2.8 wt % dispersion in H$_2$O, low-conductivity grade	-	<20 at 20 °C	1.2 - 1.8	560596-25G 560596-100G
3.0-4.0% in H$_2$O, high-conductivity grade	resistance 500 Ω/sq (4 point probe measurement of dried coating based on initial 18 μm wet thickness.) resistance 1500 Ω/sq (4 point probe measurement of dried coating based on initial 6 μm wet thickness.)	10-30 at 20 °C	1.5 - 2.5 at 25 °C (dried coatings)	655201-5G 655201-25G

Polymers for Use in Solar Cells

For a complete list of available materials, visit aldrich.com/ppoly.

Structure	Name	Molecular Weight	Optical Properties/Mobility	Prod. No.
	PTB7	average M_w 80,000-200,000	λ_{max} 680 nm	772410-100MG
	PBDTTT-CF	average M_w 53,000-83,000 by GPC	7×10^{-4} cm^2/V·s	772402-100MG
	Poly[(5,6-dihydro-5-octyl-4,6-dioxo-4H-thieno[3,4-c]pyrrole-1,3-diyl)[4,8-bis[(2-ethylhexyl)oxy]benzo[1,2-b:4,5-b′]dithiophene-2,6-diyl]]	-	λ_{max} 627 nm	773514-100MG
	PBDT-TPD	average M_n 10,000-50,000	λ_{max} 608 nm	776300-100MG
	PCPDTBT	average M_w 7,000-20,000	λ_{max} 700 nm 2×10^{-2} cm^2/V·s	754005-100MG
	PFO-DBT	average M_w 10,000-50,000	3×10^{-4} cm^2/V·s	754013-100MG
	PCDTBT	average M_w 20,000-100,000	λ_{max} 576 nm 6×10^{-5} cm^2/V·s	753998-100MG
	Poly[(9,9-di-n-octylfluorenyl-2,7-diyl)-alt-(benzo[2,1,3]thiadiazol-4,8-diyl)]	average M_n 10,000-20,000	λ_{em} = 515-535 nm in chloroform 4×10^{-3} cm^2/V·s	698687-250MG
	Poly[(9,9-dioctylfluorenyl-2,7-diyl)-co-bithiophene]	average M_n >20,000	λ_{em} = 497 nm in chloroform (at M_n = 20,000) 5×10^{-3} cm^2/V·s	685070-250MG
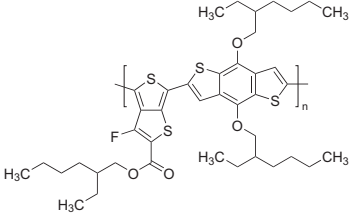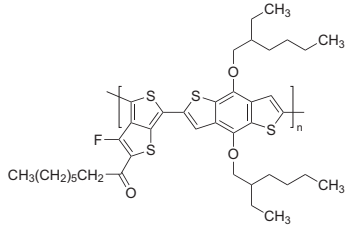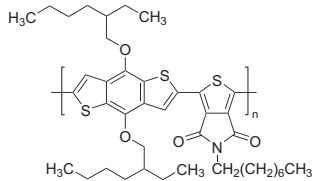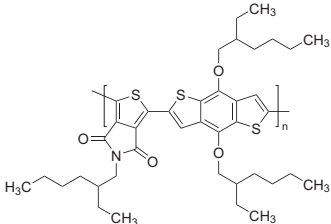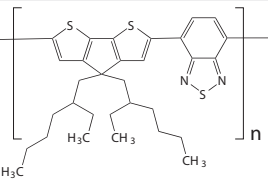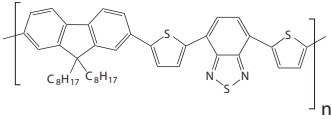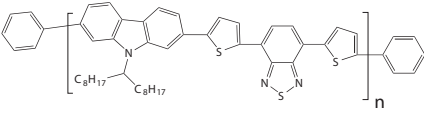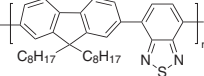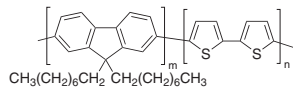
NANOMATERIALS FOR
ENERGY APPLICATIONS

Our wide range of nanomaterials includes nanopowders, dispersions, nanorods and other nanostructures for energy applications, such as:

- Photovoltaics
- Fuel cells
- Lithium-ion batteries
- Piezoelectrics
- Electronics

Nanomaterials are available in high purity and narrow size distribution.
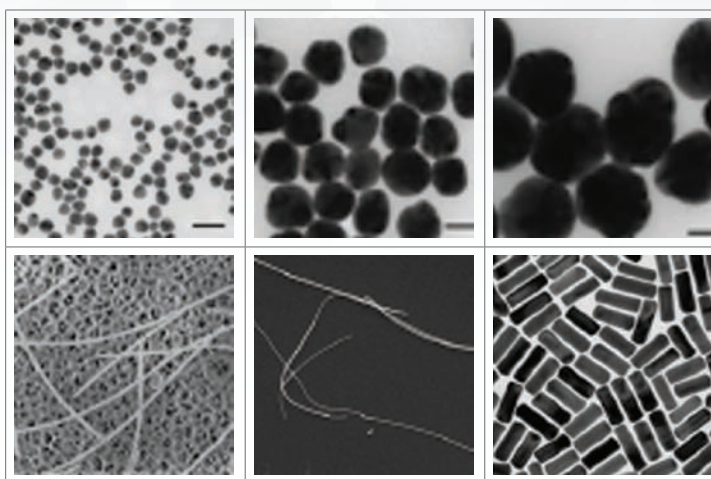
Name	Form	Specifications	Prod. No.
Barium titanate	Nanopowder	50 nm, 99.9% trace metals basis	745952
Boron nitride	Nanopowder	<150 nm, 99% trace metals basis	790532
Gold	Nanorods	25 nm diameter, absorption/650 nm, dispersion, >45 µg/mL in H_2O	771686
Iron carbon coated	Nanopowder	25 nm, 99.5% trace metals basis	746827
Platinum	Nanoparticle dispersion	3 nm, dispersion, 1,000 ppm in H_2O, 99.99% trace metals basis	773875
Silver	Nanowires	diam. × L 120–150 nm × 20–50 µm, dispersion, 0.5% in isopropyl alcohol	778095
Titanium oxide, brookite	Nanopowder	<100 nm, 99.99% trace metals basis	791326
Tungsten oxide	Nanowires	Powder, diam. × L ~50 nm × 10 µm	774537
Zinc oxide	Nanowires	Powder, diam. × L 90 nm × 1 µm	773999

For a complete list of products, visit
aldrich.com/nano

KINETIC ENERGY HARVESTING
BY MAGNETOSTRICTIVE MATERIALS

Daniele Davino
Department of Engineering
University of Sannio, 82100 Benevento, Italy
Email: davino@unisannio.it

Introduction

A significant limiting factor for wearable electronics and wireless sensors is the finite amount of energy that can be stored in on-board batteries. Currently, the most common solution is to change or recharge the batteries as often as necessary, but this strategy is neither practical nor economical. For example, the replacement or recharge of batteries used in remote wireless sensors located in far-away or difficult-to-access locations in the environment needs qualified technicians to reach the sensors. This can significantly increase maintenance costs.

Energy harvesting has the potential to be a strategic enabling concept for modern wireless electronic equipment.[1] Several methods enable harvesting energy from the environment using methods that rely on the properties of suitable multifunctional materials. For example, magnetostrictive or piezoelectric materials have constitutive relationships that directly couple mechanical and/or thermal variables to electro- or magnetic-variables.

This article discusses the physics, engineering, and application of energy harvesting using magnetostrictive materials. These devices are conceptually simple since their characteristics are based largely upon the properties of the materials. As a result device performance can be improved based on optimized materials characteristics.

Magnetostrictives (or, in general, magnetoelastic materials) have the peculiar characteristic of showing a non-negligible coupling between macroscopic mechanical variables, stress σ and strain ε, and magnetic field H and induction B.[2,3] This coupling is exploited for actuation purposes by applying a relevant magnetic field to obtain a macroscopic elongation, known as "magnetostriction." The magnetostrictive effect is exhibited by several common materials, including iron and nickel, but its macroscopic effect is limited to about 12 ppm and –50 ppm, respectively. A positive magnetostriction indicates elongation; whereas, a negative magnetostriction indicates contraction. Alloys like Terfenol (terbium-disprosium-iron alloy),[5,6] Galfenol (gallium-iron alloy),[7] and Alfenol (aluminium-iron alloy)[8] exhibit *giant magnetostriction* with elongations up to 2,000 ppm. More information on magnetostrictive materials can be found in Reference 2. Magnetic coupling can also be exploited in reverse, and is then known as the "Villari effect"[4] or inverse magnetoelastic effect.

Here a cyclic mechanical stress applied to magnetostrictive material leads to a cyclic magnetization. Since this effect is obtained over time because of the Faraday-Neumann induction law, a pick-up coil wound around the material experiences an induced voltage, and faster cycling leads to higher voltage. This forms the basis of kinetic energy harvesting (KEH) by magnetostrictive materials. If the varying stress is suitably driven by vibrations in the surroundings, then vibrational energy can be converted into electrical energy using this technique.

The first section of this article reviews the main macroscopic properties of magnetostrictive materials. The second section presents the principle of KEH using magnetostrictive materials, along with relevant material properties.

Magnetostrictive Materials Behavior

Magnetostrictive materials have some common macroscopic properties. **Figure 1** shows the uniaxial magnetostrictive behavior of a Terfenol-d rod in which the effect is measured along a field applied along the rod axis. **Figure 1A** shows the magnetostriction curves (ε vs. H). The following features are noted: 1) the hysteresis; 2) the symmetric behavior with respect to H (as two *butterfly wings*); and 3) the dependence of curves on the applied compressive stress. It is worth noting that the dependence on the applied compressive stress is somewhat complex. **Figure 1B** shows the consequence of the Villari effect: the B vs. σ plot at different applied magnetic fields. Again, it is worth noting the hysteresis (except for the case at H = 0 kA/m, because of the very small magnetic induction) and the complex behavior with respect to applied stress and magnetic field. The latter characteristic is important to infer the harvesting potentialities of the material. Indeed, the larger magnetic induction variation, ΔB at a certain stress variation, Δσ yields better energy conversion. Other magnetostrictive materials like Galfenol show similar behaviors in same conditions.

A)

B)
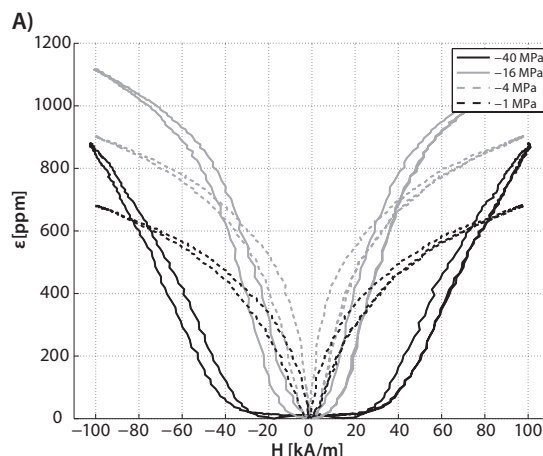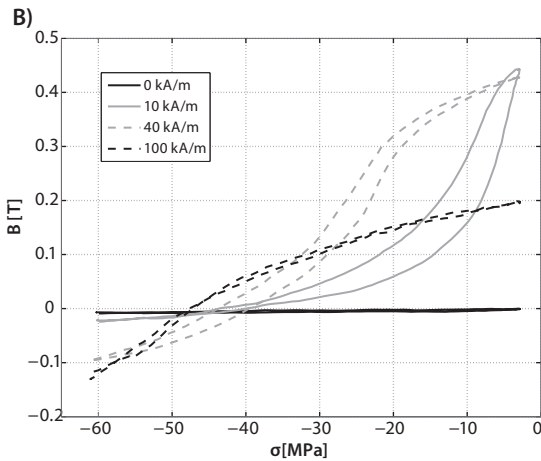
Figure 1. **A)** Magnetostriction of a Terfenol-d rod at different compressive stresses. **B)** Cyclic magnetic induction due to cyclic compressive stress (Villari effect) at different magnetic fields.

Mechanical impedance matching of the harvester is another important property of magnetostrictive materials for KEH. Materials like Terfenol or Galfenol are quite rigid with a mechanical behavior near that of bulk iron (**Figure 2**). The ideal vibrations should have high stresses and low strains, in the 0–1,000 ppm range. The availability of softer magnetoelastic materials would enable vibration harvesting with lower stresses and higher strains, in the 0.1–1% range, with a rubber-like behavior.

Another magnetoelastic material, Metglass, has been proposed for energy harvesting.[9,10] The main advantage of Metglass is that it can be laminated to achieve a higher energy density. The material is a Fe-based amorphous ribbon with excellent magnetic softness and elastic response, and its production is in principle cheaper than Fe-Ga and Fe-Tb-Dy alloys.
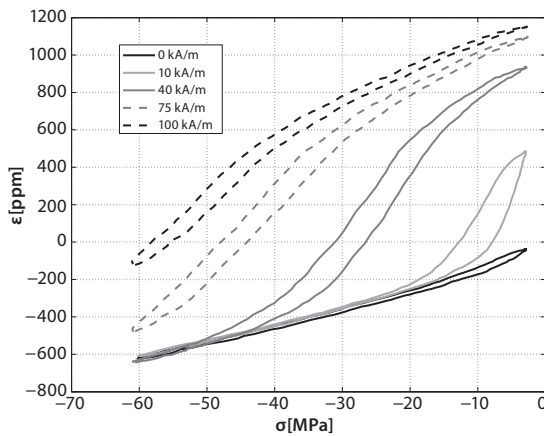
Figure 2. Mechanical characteristic of a Terfenol-d rod at different constant magnetic fields.

Kinetic Energy Harvesting Devices

The Villari effect is the principle behind the construction of any kinetic energy harvesting device based on magnetostrictive materials. The full exploitation of the process requires several functional components—from the environment to the end user (**Figure 3**). A suitable mechanical frame is needed to channel the environmental vibrations to the magnetostrictive material and, therefore, its design is of paramount importance to achieve maximum transfer of the mechanical energy.

Two conceptual implementations of the mechanical part are sketched in **Figure 4**. **Figure 4A** shows where active material is used between the source of vibrations and a reference frame.[11] The magnetostrictive rod (gray) is bound to a rigid frame and undergoes a time-variable uniform z-axis force. Then, z-axis directed compressive stress appears, and the material generates a time-variable magnetization. **Figure 4B** is suitable when a vibrating frame is available.[12] Here a magnetostrictive cantilever beam is rigidly connected to the vibrating frame on one end and to a heavier mass on the other end. Because of the induced oscillations over the mass, the material undergoes a longitudinal stress that leads to time-variable magnetization. Both methods share some common needs: a coil wrapped around the magnetostrictive material and a magnetic circuit to convey and close the magnetic flux lines. The latter is not shown in **Figure 4** for the sake of clarity.
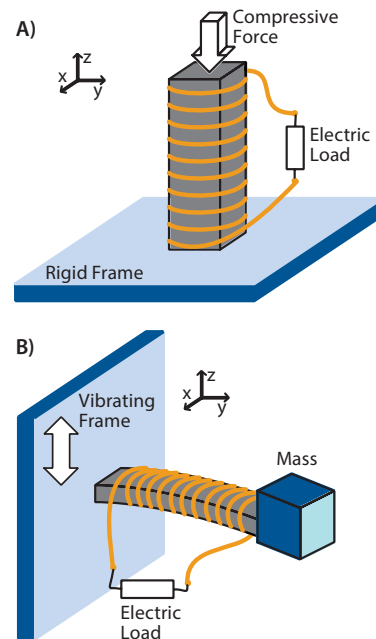
Figure 4. Two schemes for kinetic energy harvesting with magnetostrictive materials: **A)** force-driven and **B)** velocity-driven.
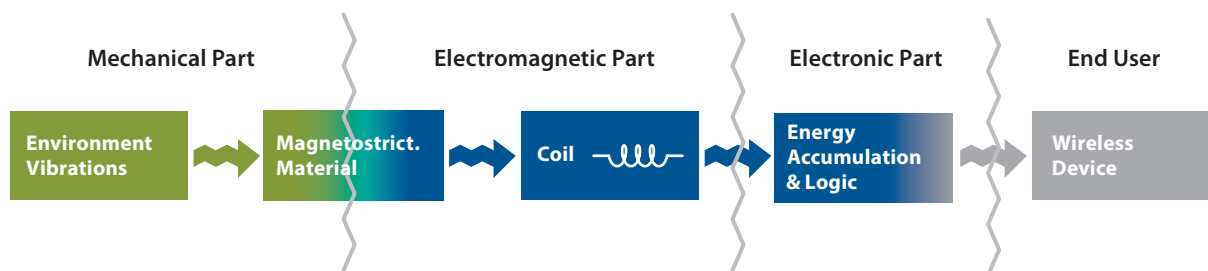
Figure 3. Schematic representation of the functional process behind the kinetic energy harvesting by magnetostrictive materials.

Both methods have their advantages. **Figure 4A** has no lower bound frequency limit, but it is usually bulkier than **Figure 4B**. The latter has a passband frequency character because of the intrinsic resonant behavior of the cantilever beam-mass system, and it operates best with vibrations around the resonant frequency of the system. Of course, several solutions have been adopted to expand the operating band and circumvent the issue.[13]

Figure 3 shows that the electronics aimed for the optimization and accumulation of electric energy represent the "electric load" of the harvesting device. Its development for KEH devices based on magnetostrictives is still in an early stage, while much research and many applications have been proposed for KEH based on piezoelectrics.[14] In general, any kinetic energy harvester is an unregulated AC power supply that must be followed by an electronic circuit with a suitable strategy in order to accumulate electric energy. Moreover, the presence of a magnetostrictive material gives some further peculiarities; however, in principle, the development could follow, *mutatis mutandis*, that has been already done for piezoelectrics.

The system can also be understood from the electro-mechanical point of view by considering it as a spring-mass-damper system. The damping is due to both the mechanical friction and the energy harvesting as the Villari effect also dissipates part of the mechanical energy.[15] The material acts as a sort of electro-mechanical transformer where on the "primary" we have complementary mechanical quantities (force and velocity), while on the "secondary" we have complementary quantities (voltage and current) at the coil terminals.[16] The voltage v(t) is proportional to the rate of change of the magnetic induction, $\partial B/\partial t$ and to usual geometrical and magnetic parameters such as the number of windings, the area of the coil, the magnetic circuit characteristics, etc. By exploiting this property, the following relation holds (**Equation 1**):

$$v(t) \propto \frac{\partial B}{\partial t} = \frac{\partial B}{\partial \sigma}\frac{\partial \sigma}{\partial t}$$

The factor $\partial\sigma/\partial t$ is related to the frequency of vibrations and it is controlled by the vibrations source. The first factor is called "piezo-magnetic coefficient" and it is a characteristic of the material, discussed in the next section.

The Piezo-magnetic Coefficient

The definition of the piezo-magnetic coefficient is the following (**Equation 2**):[17,18]

$$d_{33}^* = \left[\frac{\partial B}{\partial \sigma}\right]_H$$

In other words, it is the rate of change of *B* with respect to σ at constant H. This parameter is usually considered constant in datasheets and in linear models of the materials.[18] Such an approximation is acceptable in some cases; for example, if the material is employed in actuators where, usually, a mechanical pre-stress higher than the maximum allowed external stress is applied to the device.[19] On the other hand, if unknown dynamic conditions are considered, as in the case of energy harvesting applications, then the general definition must be exploited. The piezo-magnetic parameter, being a particular derivative function of the material characteristics, is nonlinear with respect to the (H,σ) couple and, moreover, shows hysteresis. Nevertheless, it can be obtained from a numerical derivative of the experimental hysteresis loops.[17] A result of this operation

is shown in **Figure 5** for a Terfenol-d rod. Its value is in the range of 10^{-8} m/A, as reported in literature,[20] but it is not constant and strongly depends on the applied (H,σ) couple. The maximum peak moves at higher H field for higher σ and this confirms nonlinear modeling results.[11] The maximum values are achieved at relatively low σ and H, within the ranges σ∈(−10,0) MPa and H∈(10,20) kA/m. Those ranges are useful to optimize the device and to choose the best magnetic bias and mechanical prestress. This analysis shows that any KEH device based on magnetostrictives must have a magnetic bias; for example, a suitable permanent magnet in the magnetic circuit and a tool to apply a static prestress[21] in order to reach the best working point for the piezo-magnetic parameter.
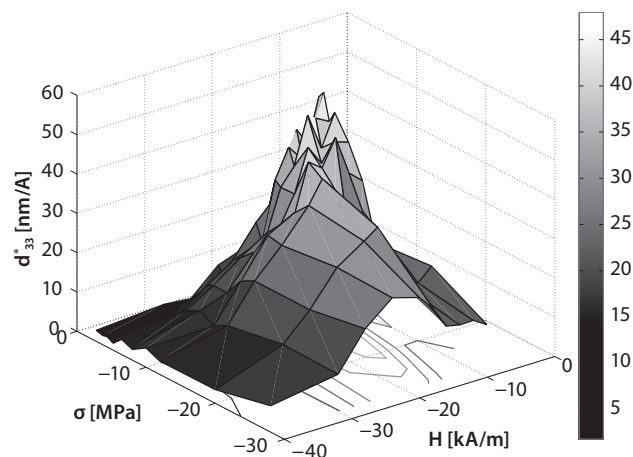
Figure 5. The piezo-magnetic coefficient of a Terfenol-d rod. Adapted from Reference 17.

Optimizing the Harvesting Cycle

The energy density of a KEH device can be calculated based on the area enclosed by the B-H cycle within the B-H plane (see **Figure 6**). This area represents an energy gain for a clockwise cycle and an energy loss for a counterclockwise cycle. A KEH device can effectively be optimized by properly selecting parameters such as magnetic bias and prestress in order to maximize the area enclosed by the B-H cycle.

It is interesting to examine the behavior of clockwise-rotating cycles in the B-H plane with respect to the magnetic cycles of the material obtained at constant stress. The plot of **Figure 6A** shows the counterclockwise magnetic characteristics of a Galfenol rod at constant stresses of 1.58 and 48.2 MPa. The lines within the cycles represent the clockwise rotating loops due to harvesting tests when a simple resistor of 1 MΩ is employed as electric load. The cyclic stress variation is between σ = 1.58 and σ = 48.2 Mpa (the time period is 1.25 s) and three different magnetic field biases (8.7 kA/m–orange, 14.8 kA/m–brown, and 23 kA/m–red) are shown. It is noted the B-H loops obtained at different bias fields are within the range of the magnetic characteristics, as it was theoretically foreseen.[22] Moreover, this is still true in **Figure 6B** where different resistors, at H = 14.8 kA/m, are employed. The loops are wider for smaller resistors because a larger current circulates in the pick-up coil and a larger magnetic field variation is then introduced. This result shows efforts to improve material harvesting behavior should concentrate on the static magnetic characteristics at different stresses as much as possible in order to improve the available area among limit cycles.
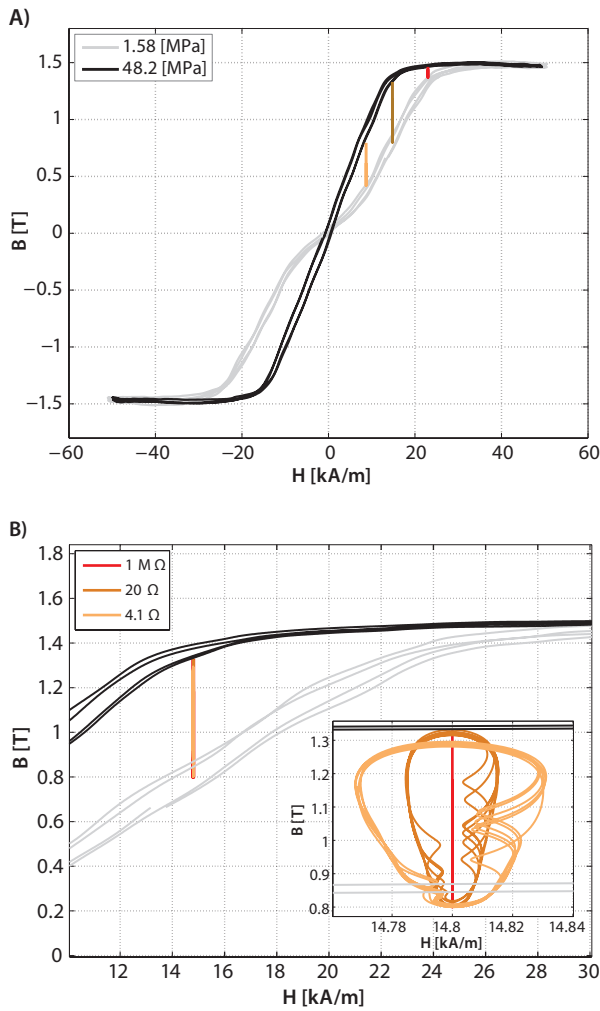
Figure 6. A) Magnetic characteristics of a Galfenol rod at 1.58 Mpa (black line) and 48.2 MPa (gray line) constant stresses; harvesting cycles lines, T = 1.25 s, H = 8.7 kA/m–orange, H = 14.8 kA/m–brown and H = 23 kA/m–red, R = 1 MΩ. **B)** Harvesting cycle lines: T = 1.25 s, R = 4.1 Ω–orange, R = 20 Ω–brown and R = 1 MΩ–red).

Conclusions

Kinetic energy harvesters based on magnetostrictives are simple devices in which the performance is mainly influenced by characteristics such as the piezo-magnetic coefficient and the magnetic B-H cycle behavior at constant applied stresses. New improved material can improve the performance in energy harvesting applications. The macroscopic analysis of the device suggests the research should focus on maximizing the piezo-magnetic coefficients: create more space for harvesting cycles within static limit cycles in the magnetic plane.

Acknowledgment

References

(1) Kazmierski, Beeby, Eds. *Energy Harvesting Systems* (Springer).
(2) Engdahl, G., Ed. *Handbook of Giant Magnetostrictive Materials*, (Academic, New York) **2000**.
(3) du Trémolet de Lacheisserie, Ed. *Magnetism – Materials and Applications, Vol. II*, (Springer).
(4) Lee, E.W. *Reports on Progress in Physics* **1955**, *18*, 184–227.
(5) Clark, A.E.; Teter, J.P.; McMasters, O.D. *Journal of Applied Physics* **1988**, *63*(8), 3910–3912.
(6) Clark, A.E.; Wun-Fogle, M.; Restorff, J.B.; Lindberg, J.F. *IEEE Trans on Mag* **1992**, *28*(5), 3156–3158.
(7) Clark A.E.; Hathaway, K.B.; Wun-Fogle, M.; Restorff, J.B.; Lograsso, T.A.; Keppens, V.M.; Petculescu, G.; Taylor, R.A. *J. Appl. Phys.* **2003**, *93*, 8621.
(8) Davis, C.M.; Ferebee, S.F. *J. Acoust. Soc. Am* **1956**, *28*, 286.
(9) Wang, L.; Yuan, F.G. *Smart Materials and Structures* **2008**, *17*, 045009.
(10) Zucca, M.; Bottauscio, O.; Beatrice, C.; Fiorillo, F. *IEEE Trans on Mag* **2011**, *47*(10), 4421–4424.
(11) Davino, D.; Giustiniani, A.; Visone, C. *IEEE Trans on Mag* **2009**, *45*(10), 4108–4111.
(12) Ueno, T.; Yamada, S. *IEEE Trans on Mag* **2011**, *47*(10), 2407–2409.
(13) Cottone, F.; Vocca, H.; Gammaitoni, L. *Phys Rev Lett* **2009**, *102*, 080601.
(14) Guyomar, D.; Lallart, M. *Micromachines* **2011**, *2*, 274–294.
(15) Davino, D.; Giustiniani, A.; Visone, C.; Adly, A.A. *J of App Phys* **2011**, *109*, 07E509.
(16) Davino, D.; Giustiniani, A.; Visone, C. *IEEE Trans on Ind Electronics* **2011**, *58*(6), 2556–2564.
(17) Davino, D.; Giustiniani, A.; Visone, C. *Physica B: Condensed Matter* **2011**, *407*(9), 1427–1432.
(18) Moffett, M.B.; Clark, A.E.; Wun-Fogle, M.; Linberg, J.; Teter, J.P.; McLaughlin, E.A. *J. Acoust. Soc. Am.* **1991**, *89*(3), 1448–1455.
(19) Kellogg, R.; Flatau, A. *J of Intell. Mat. And Struct.* **2004**, *15*.
(20) Zhao, X.; Lord, D.G. *J of Appl. Phys.* **2006**, *99*, 08M703.
(21) Davino, D.; Giustiniani, A.;Visone, C. *Magnetoelastic Energy Harvesting: Modeling and Experiments, Smart Actuation and Sensing Systems - Recent Advances and Future Challenges*, Berselli, Dr. Giovanni, Ed., ISBN: 978-953-51-0798-9, InTech. **2012**.
(22) Davino, D.; Giustiniani, A.; Visone, C. *J of App Phys* **2009**, *105*, 07A939.

For questions, product data, or new product suggestions, contact us at **matsci@sial.com**.

119

Piezoelectric Materials

For a complete list of available materials, visit aldrich.com/periodic.

Name	Purity (%)	Particle Size	Form	Prod. No.
Barium strontium titanium oxide	>99	<100 nm (APS)	nanopowder	633828-25G 633828-100G
Barium titanate(IV)	99.995	-	powder	256552-10G
	99.5	<2 µm	powder	338842-100G 338842-500G
	99.9	50 nm (SEM)	nanopowder (cubic)	745952-100G
Barium zirconate	-	<10 µm	powder	383309-250G
Lanthanum calcium borate	99.9	-200 mesh	powder	772666-25G
Lead magnesium niobate	≥99	-	powder	672874-25G
Lead(II) titanate	≥99	<5 µm	powder	215805-250G
Lead(II) zirconate	99	−325 mesh	powder	398888-50G
Potassium niobate	-	-	powder	541206-25G
Zinc niobate	97	-	powder	548588-50G

Magnetic Alloys

For a complete list of available materials, visit aldrich.com/magnetic.

Name	Composition	Size (L x W) (mm)	Form	Prod. No.
Aluminum nickel cobalt alloy 11	Al / Ni / Co	13 × 6	disc	692867-2EA
Aluminum nickel cobalt alloy 5	Al / Ni / Co	13 × 6	disc	692875-3EA
Aluminum nickel cobalt alloy 1	Al / Ni / Co	13 × 6	disc	692883-3EA
Neodymium-iron-boron alloy 30/150	Nd / Fe / B	13 × 6	disc	693782-3EA
Samarium cobalt	Sm_2Co_7	-	powder	339229-50G
Samarium-cobalt alloy 18	$SmCo_5$	10 × 6	disc	692859-3EA
Samarium-cobalt alloy 24	Sm_2Co_{17}	10 × 6	disc	692840-3EA
Samarium-cobalt alloy 30	Sm_2Co_{17}	10 × 6	disc	692832-3EA

Rare-earth Metals

For a complete list of available materials, visit aldrich.com/periodic.

Name	Purity (%)	Resistivity (µΩ-cm)	Form	Prod. No.
Cerium, Ce	99.9 trace rare earth metals basis	73 (20 ℃)	chips chunks	461210-50G
	99.9 trace rare earth metals basis	73 (20 ℃)	ingot	261041-25G 261041-100G
	99.9 trace rare earth metals basis	73 (20 ℃)	powder	263001-10G
Dysprosium, Dy	99.9 trace rare earth metals basis	89 (20 ℃)	chips	263028-5G
	99.9 trace rare earth metals basis	89 (20 ℃)	ingot	261076-10G
Erbium, Er	99.9 trace rare earth metals basis	86 (20 ℃)	chips	263052-10G
	99.9 trace rare earth metals basis	86 (20 ℃)	foil	693685-1EA
	99.9 trace rare earth metals basis	86 (20 ℃)	ingot	261084-10G
	99.9 trace rare earth metals basis	86 (20 ℃)	powder	263044-5G
Europium, Eu	99.9 trace rare earth metals basis	81 (20 ℃)	chips in mineral oil	457965-5G
	99.9 trace rare earth metals basis	81 (20 ℃)	ingot	261092-1G
Gadolinium, Gd	99.9 trace rare earth metals basis	126 (20 ℃)	chips	263087-10G 263087-50G
	99.9 trace rare earth metals basis	126 (20 ℃)	foil	693723-1EA
	99.99 trace rare earth metals basis	126 (20 ℃)	ingot	691771-10G
	99.9 trace rare earth metals basis	126 (20 ℃)	ingot	261114-10G
	99 trace rare earth metals basis	126 (20 ℃)	powder	263060-5G
Holmium, Ho	99.9 trace metals basis	-	chips	457957-5G
	99.9 trace rare earth metals basis	-	foil	693693-1EA
	99.99 trace rare earth metals basis	-	dendritic pieces	755974-1G

Name	Purity (%)	Resistivity (μΩ-cm)	Form	Prod. No.
Lanthanum, La	99.9 trace rare earth metals basis	54	ingot (under oil)	261130-25G
	99.9 trace rare earth metals basis	54	pieces	263117-25G
	99.9 trace rare earth metals basis	54	powder	263109-25G
Lutetium, Lu	99.9 trace rare earth metals basis	54 (20 ℃)	ingot	261149-1G
	99.9 trace rare earth metals basis	54 (20 ℃)	foil	693650-1EA
Neodymium, Nd	99.9 trace rare earth metals basis	64.0 (20 ℃)	chips	263141-25G
	99.9 trace rare earth metals basis	64.0 (20 ℃)	ingot (in mineral oil)	261157-25G
	≥99 trace rare earth metals basis	64.0 (20 ℃)	powder	460877-10G
Praseodymium, Pr	99.9 trace rare earth metals basis	68 (20 ℃)	ingot	261173-10G
	99.9 trace metals basis	68 (20 ℃)	powder	263176-5G
Samarium, Sm	99.9 trace rare earth metals basis	91.4 (0 ℃)	chips	261211-10G
	99.9 trace rare earth metals basis	91.4 (0 ℃)	foil	693731-1EA
	99.9 trace rare earth metals basis	91.4 (0 ℃)	ingot	263184-10G
	99 trace rare earth metals basis	91.4 (0 ℃)	(powder or filings)	261203-1G 261203-10G 261203-50G
Scandium, Sc	99.9 trace rare earth metals basis	50.5 (0 ℃)	dendritic pieces	261246-1G
	99.9 trace rare earth metals basis	50.5 (0 ℃)	powder	261262-250MG 261262-1G
Terbium, Tb	99.9 trace rare earth metals basis	116 (20 ℃)	chips	263206-1G 263206-5G
	99.9 trace rare earth metals basis	116 (20 ℃)	foil	693715-1EA
Thulium, Tm	99.9 trace metals basis	90 (20 ℃)	chips	262978-1G
Ytterbium, Yb	99.9 trace rare earth metals basis	28 (20 ℃)	chips	262986-5G
	99.9 trace metals basis	28 (20 ℃)	chunks	548804-5G
	99.9 trace rare earth metals basis	28 (20 ℃)	foil	693669-1EA
	99.9 trace rare earth metals basis	28 (20 ℃)	ingot	261300-5G
	≥99.9 trace rare earth metals basis	28 (20 ℃)	powder	466069-2G
Yttrium, Y	99.9 trace metals basis	57 (20 ℃)	chips	262994-5G 262994-25G
	99.9 trace metals basis	57 (20 ℃)	dendritic pieces	451347-1G
	99.8 trace rare earth metals basis	57 (20 ℃)	foil	693642-1EA
	99.9 trace rare earth metals basis	57 (20 ℃)	ingot	261319-10G 261319-50G
	99.5 trace rare earth metals basis	57 (20 ℃)	powder	261327-5G 261327-25G

LITHIUM-ION BATTERY PERFORMANCE:
DEPENDENCE ON MATERIAL SYNTHESIS AND POST-TREATMENT METHODS

Dr. Qifeng Zhang, Mr. Evan Uchaker, and Dr. Guozhong Cao*
Department of Materials Science and Engineering
University of Washington
Seattle, WA 98195-2120
*Email: gzcao@u.washington.edu

Introduction

Lithium-ion batteries represent a group of electrochemical devices used for electricity storage and have attracted a lot of attention in the past two decades due to their portability, rechargeability, and low cost. The major effort on lithium-ion batteries (LIBs) at present is to optimize the materials that form the cathode or anode films to increase the battery capacity to reach the theoretical maximum with enhanced cyclic stability in relation to lithium-ion intercalation and deintercalation. It has been proven that both the capacity and stability of LIBs are closely related to the materials being used to form the electrodes. More specifically, the battery capacity and stability greatly rely on chemical composition, microstructure, crystallinity, and defects of the electrode materials. This review features several materials involved in our work on LIBs. The performance of LIBs can be improved to a large extent by: (1) tailoring the microstructure; (2) controlling the crystallinity of electrode materials; and/ or (3) introducing suitable defects to the materials, thereby enhancing the electron and mass transport to improve the battery stability.

MnO$_2$ Nanowall Arrays

One of the most outstanding advantages of nanostructured materials is that they can form porous films that result in extremely high internal surface area. This is particularly important for electrochemical devices such as LIBs which involve a faradaic reaction at the solid/liquid interface formed by electrode film and liquid electrolyte. MnO$_2$ is one of several commonly used LIB materials. However, MnO$_2$ (Aldrich Prod. No. 529664) microsized particles prepared using conventional slurry methods to form electrode film demonstrate relatively low discharge capacities of ~120 mAh/g.[1] MnO$_2$ nanowall arrays are a novel nanostructure and reportedly achieve both a significantly higher discharge capacity and good cyclic stability due to their large surface area and short pathways for lithium-ion diffusion. The approximately amorphous phase structure of the nanowalls results from the cathodic electrodeposition method used to fabricate the electrode film.[2]

The MnO$_2$ nanowall arrays were prepared using an electrodeposition method from a solution containing 0.1 M manganese acetate (Aldrich Prod. No. 330825) and sodium sulfate (Sigma-Aldrich Prod. No. 793531) under a constant voltage ranging from −1.2 to 2.2 V for 15 min. The MnO$_2$ nanowall arrays were grown on a platinum foil substrate at the cathodic side; a separate platinum foil was used in anode of the deposition system. The deposited film was washed with deionized water and then air-dried without any further treatment. **Figure 1** shows a typical SEM image of the as-prepared MnO$_2$ nanowall array film. It reveals the porous structure of the electrode film is comprised of vertically grown MnO$_2$ walls of 50–100 nm thickness. The film was also characterized using X-ray diffraction and found to be approximately amorphous, although the peaks presented a slight match with those of ε-MnO$_2$.[2] The thermogravimetric analysis revealed the as-produced nanowall arrays had a chemical composition of MnO$_2 \cdot$nH$_2$O with n≈0.5.
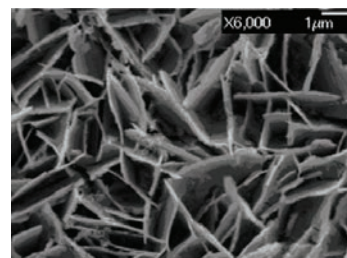
Figure 1. Morphology and structure of MnO$_2$ nanowall arrays produced from cathodic electrodepostion.[2]

Formation of the nanowall structure is a result of water electrolysis-induced precipitation of MnO$_2$ at the cathode side, where H$_2$ gas bubbles generated due to water electrolysis play an important role in the formation of the porous nanowall structure.[2,3] The height of the nanowalls is dependent on both the applied bias and the deposition time. For example, the use of −1.2 V for 15 min. led to ~500 nm high nanowalls, which increased to 2.5 μm with the applied bias of −1.8 V for 15 min. However, the increase in nanowall height didn't result in an increase in the internal surface area of the electrode film due to an increase in the nanowall thickness. The nanowall thickness is also a function of the concentration of the solution. High concentration generally results in thick nanowalls and leads to low internal surface area.[3]

Electrochemical characterization of the MnO$_2$ nanowall array revealed excellent charge/discharge properties in less crystallized nanowall structures. The nanowall array of ~2.5 μm height (i.e., film thickness) deposited at −1.8 V presented an initial discharge capacity of 270 mAh/g at a rate of 0.1 mA/cm^2 (corresponding to a current density of 76 mA/g). The capacity remained as high as 220 mAh/g even over 50 cycles, which significantly exceeds the typical capacity of 120 mAh/g for a traditional MnO$_2$ electrode. These results indicate MnO$_2$ nanowall arrays are a

promising material for lithium-ion intercalation/deintercalation due to both their high capacity and good stability,[2] which are attributed to: (1) the large surface area of the porous nanowall structure; (2) short pathways for lithium-ion diffusion; and (3) the approximately amorphous structure of the nanowalls, making the electrode film less well packed and, therefore, possess a greater capacity for structural accommodation during lithium-ion intercalation/deintercalation.

TiO$_2$ Nanotube Arrays

Annealing Temperature Effect

TiO$_2$ nanotube arrays have generated significant interest for use in electrochemical and photoelectrochemical devices due to their ordered one-dimensional structure that possesses a large internal surface area and may provide direct pathways for ion and electron transport.[4,5] The significant attention received by TiO$_2$ nanotube arrays is also attributed to their ease of fabrication through a simple anodization method. The nanotube diameter, length, and wall thickness can be readily controlled by adjusting the recipe of electrolyte, applied voltage, and time for anodization. For LIB application, it has been found that in addition to the structural parameters such as nanotube diameter, length, and distribution density, both the capacity and the cyclic stability of an electrode film consisting of TiO$_2$ nanotube arrays are also affected by the post-treatment parameters.[6,7]

Figure 2A shows a typical SEM image of TiO$_2$ nanotube array produced using anodization with an electrolyte containing 0.1 M KF and 1.0 M NaHSO$_4$, at a constant potential of 20 V, for 1 hr. The nanotubes are ~100 nm in diameter and 1.1 μm in length. The direct use of the as-deposited TiO$_2$ nanotube array in a lithium-ion battery results in an initial discharge capacity of ~202 mAh/g, which degrades very quickly to 40 mAh/g after 50 cycles.[7] The poor cyclic stability is attributed to the amorphous phase of the as-deposited TiO$_2$ nanotube array, which results in an irreversible lithium-ion intercalation and deintercalation corresponding with literature results on amorphous TiO$_2$.[8] Heat treatment of TiO$_2$ nanotube arrays is an effective method for increasing both the capacity and the cyclic stability of the electrode film. **Figure 2B** shows the result of samples annealed in N$_2$ at 300 °C, 400 °C, and 500 °C. All the annealed samples present much better cyclic stability compared to the as-prepared sample. Although the initial capacities for the samples annealed at 400 °C and 500 °C are relatively low compared to the unannealed material, the capacities of the annealed samples are significantly higher after 50 cycles. The optimal temperature for heat treatment, 300 °C, leads to a high initial capacity (~240 mAh/g); a good capacity of 148 mAh/g is retained even after 50 cycles. The decrease in capacity of samples annealed at 400 °C and 500 °C compared to the sample annealed at 300 °C, is attributed to the reduced internal surface area.[6] Therefore, to achieve the best LIB performance with anodization-produced TiO$_2$ nanotube arrays, annealing at a high temperature is necessary to improve the cyclic stability. However, there is an optimal temperature which, on one hand, ensures the nanotube arrays gain the desired crystallinity and, on the other hand, makes sure the nanotube arrays possess large internal surface area for highly efficient faradaic reaction.
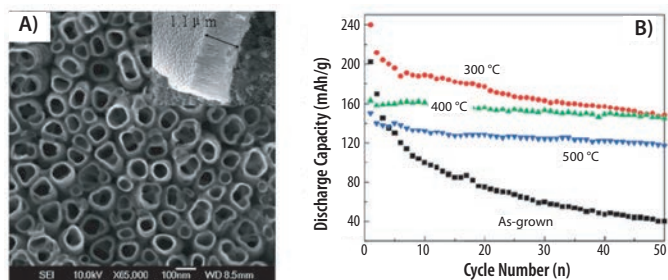
Figure 2. A) SEM image of a TiO$_2$ nanotube array and **B)** the dependence of discharge capacity and cyclic stability on annealing temperature of the TiO$_2$ nanotube array.[6]

Annealing Atmosphere Effect

In addition to the annealing temperature, the LIB performance of TiO$_2$ nanotube arrays is also sensitive to the annealing atmosphere. Compared to annealing in N$_2$ mentioned above, annealing the anodization-produced TiO$_2$ nanotube array in CO results in improved battery capacity.

The comparison was carried out between two TiO$_2$ nanotube array samples annealed in N$_2$ and CO, respectively, at 400 °C for 3 hr. **Figure 3** shows the charge/discharge properties and the cyclic stability of the samples annealed in N$_2$ and in CO. It can be seen that the initial capacity of electrode film consisting of a TiO$_2$ nanotube array annealed in CO is higher than the sample annealed in N$_2$ (~223 mAh/g in CO vs. 164 mAh/g in N$_2$). The cyclic stability of the sample annealed in CO is similar to that of the sample annealed in N$_2$ and, as a result, the discharge capacity of the sample annealed in CO after 50 cycles is significantly higher than the sample annealed in N$_2$. XPS analysis reveals that, due to the reduction capability of CO, the annealing in CO results in the Ti^{3+} state surface defect and Ti-carbon species in the TiO$_2$. The presence of the Ti^{3+} surface defect and Ti-carbon species appears to enhance the electron transport of the TiO$_2$ nanotubes and, thus, facilitates the electrochemical reaction with respect to the lithium-ion intercalation/deintercalation process. The impedance spectra show the sample annealed in CO possesses significantly lower resistance than that annealed in N$_2$,[7] which is consistent with the XPS analysis.
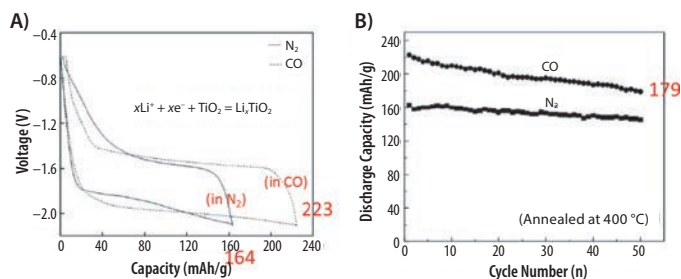
Figure 3. Enhanced LIB performance of TiO$_2$ nanotube arrays annealed in CO. **A)** The first cycle charge/discharge properties and **B)** cyclic stability of TiO$_2$ nanotube arrays annealed in N$_2$ and CO.[7]

For questions, product data, or new product suggestions, contact us at matsci@sial.com.

123

V$_2$O$_5$ Xerogel Films

V$_2$O$_5$ is a rather important material that has been extensively studied for LIB application due to its layered structure. V$_2$O$_5$ xerogel films easily can be produced from a V$_2$O$_5$ solution by dissolving V$_2$O$_5$ powder (Aldrich Prod. No. 204854) in an aqueous solution containing H$_2$O$_2$ and drop-casting the solution onto a substrate to form a wet film.[9] The heat treatment of the wet film results in the formation of the V$_2$O$_5$ xerogel film. It has been also found that different atmospheres employed to heat-treat the V$_2$O$_5$ wet films may significantly influence the LIB performance. **Figure 4** shows the difference in the V$_2$O$_5$ films annealed in air and in N$_2$. It should be emphasized that both V$_2$O$_5$ films were prepared with the same precursor solution and procedure of drop-casting the V$_2$O$_5$ solution onto FTO glass substrates.[10] Optical absorption spectra characterization revealed that, compared with the sample annealed in air, the film annealed in N$_2$ presented a longer cut-off in wavelength, meaning a relatively narrower band gap of the latter (2.28 eV for annealed in N$_2$ vs. 2.37 eV for annealed in air), as seen in **Figure 4A**. The yellow color of the air-annealed sample and the dark green color of the N$_2$-annealed sample infers that the air-annealed V$_2$O$_5$ film primarily contains V^{5+}, while the N$_2$-annealed sample contains some vanadium in lower valences, such as V^{4+} and V^{3+}.
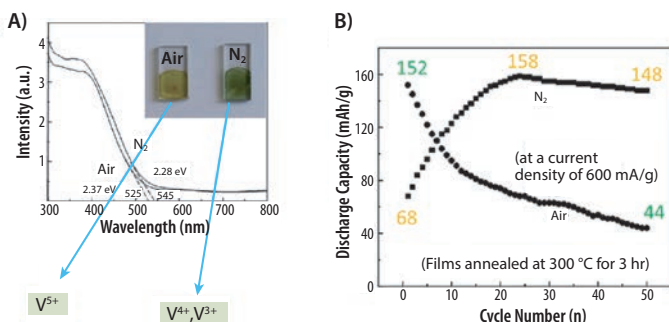
Figure 4. A comparison of the lithium-ion battery performance between V$_2$O$_5$ films annealed in air and in N$_2$: **A)** optical absorption spectra and **B)** lithium-ion cyclic properties of V$_2$O$_5$ films annealed in air and N$_2$.[10]

Figure 4B shows a comparison of the cyclic properties of the samples annealed in air and in N$_2$ over the first 50 cycles. The sample annealed in air presents an initial discharge capacity of ~152 mAh/g but degraded very quickly to only 44 mAh/g at 50 cycles. In contrast, the sample annealed in N$_2$ shows a low initial capacity of ~68 mAh/g; however, the capacity increased significantly during the first 24 cycles and reached 158 mAh/g. The capacity remained at a high level afterward, dropping a mere 10 mAh/g after 50 cycles, which indicates good cyclic stability of the N$_2$-annealed sample.

It is believed that annealing the V$_2$O$_5$ film in N$_2$ results in better performance than the film annealed in air due to the presence of low valence V ions, which induce impurity energy levels in the band gap of V$_2$O$_5$ and lead to the enhancement in capability for electron transport. This is the same as the case of TiO$_2$ nanotubes annealed in CO mentioned previously. The films annealed in different atmospheres were also analyzed with electrochemical impedance spectra, which revealed the electrode resistance of the film annealed in N$_2$ is about 30% lower than that of the film annealed in air.[10]

Besides annealing in N$_2$, Mn doping has also been proven effective in creating low valence V ions in the V$_2$O$_5$ film, thereby enhancing LIB performance.[11] The introduction of Mn in V$_2$O$_5$ is achieved by adding a soluble Mn salt (e.g., manganese acetate) into the aforementioned V$_2$O$_5$ solution during film preparation. **Figure 5** shows the discharge capacities of both a pure V$_2$O$_5$ film and an Mn-doped V$_2$O$_5$ film over the first 50 cycles. Both films were annealed at 250 °C for 3 hr in air. The initial capacities, 138 mAh/g for the doped film and 145 mAh/g for the undoped film, are very close. However, the Mn-doped film presented much better cyclic stability compared to the undoped film. After 50 cycles the capacity of Mn-doped film remained 135 mAh/g; whereas it dropped to 86 mAh/g for the undoped film. The improved cyclic stability is due to Mn doping of the V$_2$O$_5$. XPS analysis revealed there are coexistent V^{5+} and V^{4+} in the Mn-doped V$_2$O$_5$, although it is not clear how the Mn dopant results in low valence V.
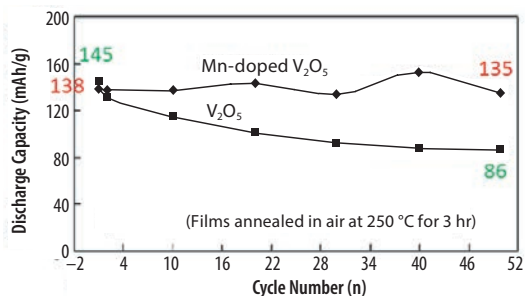
Figure 5. Enhanced cyclic stability of Mn-doped V$_2$O$_5$ film.[11]

Nanostructured V$_2$O$_5$

V$_2$O$_5$ Nanofibers

Electrospinning is a widely applied technique for the fabrication of one-dimensional (1D) nanostructures. An outstanding feature of 1D nanostructures developed for LIB is the resulting electrode films represent a good compromise between internal surface area and porosity. Electrode films comprised of 1D nanostructures possess both a large internal surface area (although it is usually smaller compared to that of nanoparticle films), suitable porous structure, and higher porosity than that of nanoparticle films. The high porosity is important as it allows the electrolyte to diffuse efficiently. Nanostructured V$_2$O$_5$ in the form of nanofibers is one example that demonstrates an electrode film with 1D nanostructures can outperform dense films or films comprised of nanoparticles.

V$_2$O$_5$ nanofibers can be prepared using electrospinning techniques by employing a V$_2$O$_5$ solution. In order to form the fiber structure, a polymer additive is often used to increase the viscosity of the V$_2$O$_5$ solution. Poly(vinylpyrrodidone) (PVP) (**Aldrich Prod. Nos.** 234257, 856568, and 437190) is a readily available polymer proven to work for this purpose.[12] The polymer additive is removed from the product by sintering the nanofiber powder at high temperatures (~500 °C) in air. **Figure 6A** shows SEM images of V$_2$O$_5$ nanofibers prepared with an electrospinning method. The image indicates the nanofibers are: (1) several tens of micrometers in length and ~350 nm in diameter after sintering; (2) comprised of interconnected V$_2$O$_5$ nanocrystals; and (3) the resultant film is well structured to provide large internal surface area and porosity. BET characterization revealed the surface area of the as-prepared V$_2$O$_5$ nanofibers to be 97 m^2/g.

A)

B)
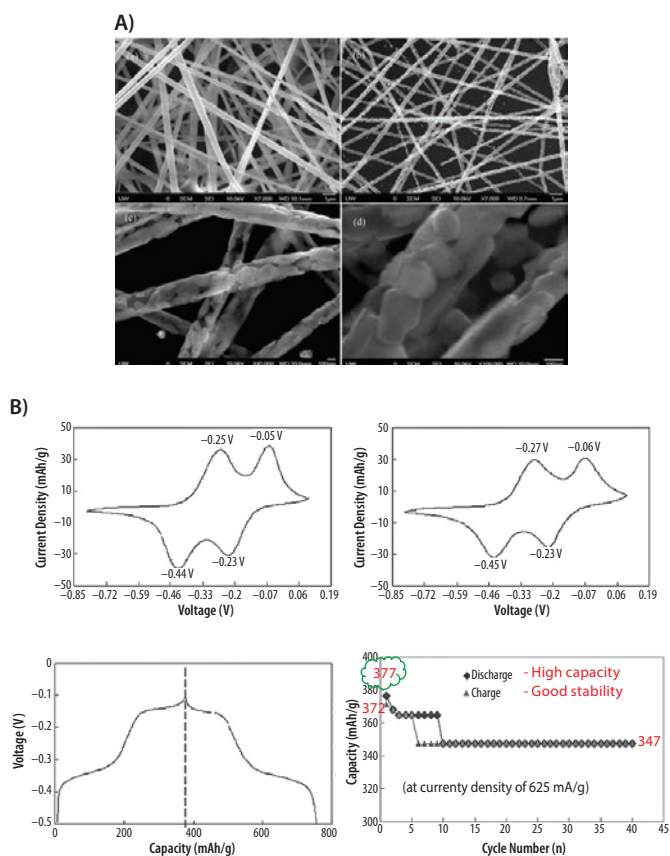
Figure 6. V_2O_5 nanofibers prepared with an electrospinning method for lithium-ion battery. **A)** SEM images of V_2O_5 nanofibers before and after being annealed (at 500 °C for 1 hr in air). **B)** Cyclic voltammetry curves and charge/discharge properties of the V_2O_5 nanofibers at a current density of 625 mA/g.[12]

LIB performance of the V_2O_5 nanofibers is shown in **Figure 6B**. Two anodic oxidation peaks located at –0.25 V and –0.05 V (vs. Ag/AgCl) corresponding to Li^+ deintercalation, and two cathodic reduction peaks located at –0.44 V and –0.23 V corresponding to Li^+ intercalation clearly can be seen on the cyclic voltammogram curves.[12] All these redox peaks are well defined. The voltages of redox peaks show only a negligible shift even after 40 cycles. The current densities also change only slightly. From the cyclic test, it can be seen that after the 9th cycle the discharge capacity remains at a high capacity (~347 mAh/g), which implies excellent cyclic stability and reversibility of the V_2O_5 nanofiber electrode film. The superior performance of the V_2O_5 nanofiber electrode, which is significantly better than that of the aforementioned V_2O_5 xerogel films and other V_2O_5 nanostructures (such as V_2O_5 nanotube arrays, nanocable arrays, and nanorod arrays[13,14]), is believed to arise from the high internal surface area provided by the nanofibers and ideal porosity of the electrode film comprised of these nanofibers. The high porosity enables the lithium ion intercalation and deintercalation to take place efficiently.

Nanoporous V_2O_5 Films

The advantage of nanostructured materials for LIB are further demonstrated by employing V_2O_5 films prepared with the same V_2O_5 solution used for drop-casting described previously[10,11] using a cathodic deposition method.[15] The films were deposited onto FTO glass substrates under a voltage of –2.4 V. Such a voltage results in water electrolysis and generates H_2 gas bubbles at the cathode, which is believed to cause the formation of nanosized pores in the films. The films were annealed at 500 °C to achieve desired crystallinity.

Figure 7A shows a typical SEM image of the as-prepared nanoporous V_2O_5 film. It reveals the film is comprised of nanosized crystallites of 20–30 nm diameter and contains pores on the order of 10 nm. While no other special structural feature is found on the film, interestingly, it delivered an extremely high initial capacity of ~402 mAh/g, and even after 200 cycles the capacity remained as high as 240 mAh/g (**Figure 7B**).[15] Such capacities are more than twice as high as that of V_2O_5 xerogel films[10] and, to some extent, are also higher than that of V_2O_5 nanofibers produced using electrospinning.[12] The cathodic deposition method is very simple, low cost, reliable, and compatible with mass production. The film also demonstrated good capacity at high current densities. For example, it showed a capacity of ~120 mAh/g at 10.5 A/g (70 C) (**Figure 7C**). The high internal surface area of the V_2O_5 nanoporous films is believed to be the main reason for the superb LIB performance. However, in addition to high surface area, the presence of tetravalent vanadium ions (V^{4+}) in the as-deposited film (before annealing) may also contribute to the high performance of V_2O_5 nanoporous films by catalyzing the growth of the V_2O_5 film during the electrochemical deposition process and enabling the formation of hierarchically structured electrode film with stacking flakes consisting of V_2O_5 nanoparticles.[15]

A)

B) **C)**
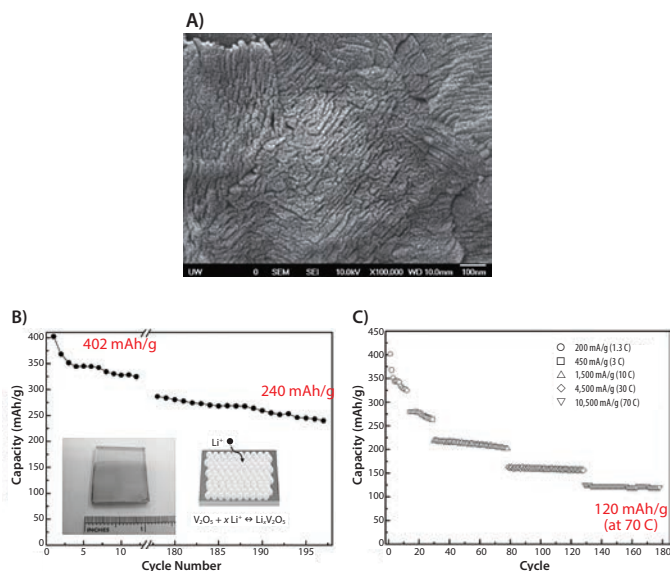
Figure 7. Nanoporous V_2O_5 film for lithium-ion battery application: **A)** SEM image of nanoporous V_2O_5 film; **B)** cyclic capacities at a current density of 200 mA/g (1.3 C); and **C)** cyclic capacities at different current densities up to 10.5 A/g (70 C).[15]

LiFePO$_4$/C Nanocomposites

LiFePO$_4$/C nanocomposites are another example demonstrating the optimization of post-treatment parameters is critically important to achieving high performance in LIBs. The fabrication of LiFePO$_4$/C nanocomposites was carried out by: (1) adding L-ascorbic acid ($C_6H_8O_6$) to a solution containing lithium hydroxide monohydrate (LiOH·H$_2$O, Aldrich Prod. No. 254274), ferric nitrate Fe(NO$_3$)$_3$·9H$_2$O (Aldrich Prod. No. 529303), and phosphoric acid (H$_3$PO$_4$; (2) refluxing the mixture at 60 °C for 1 hr to attain a solution of LiFePO$_4$ (Aldrich Prod. No. 759546) with carbon; and (3) drop-casting and annealing the films in N$_2$.[16] L-ascorbic acid plays a role in this synthesis by reducing the iron ions from Fe^{3+} to Fe^{2+} and also serving as a source of carbon.

Figure 8 shows the SEM characterization of LiFePO$_4$/C nanocomposite films annealed at different temperatures (500 °C, 600 °C, and 700 °C) and the XRD patterns of the films at increasing annealing temperature. The as-synthesized LiFePO$_4$ were found to be amorphous and adopt an olivine phase with a crystallite size of ~20 nm when the temperature reached 600 °C. The crystallite size increased to ~30 nm at 800 °C. No peaks corresponding to carbon were seen in the XRD. This implies the carbon is amorphous and its presence does not bring any detectable influence on the crystal structure of LiFePO$_4$. A careful EDX analysis revealed the carbon in the films takes the form of particles homogenously distributed on the surface of LiFePO$_4$ crystallites.[16]
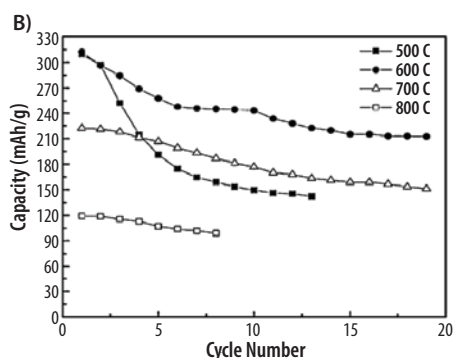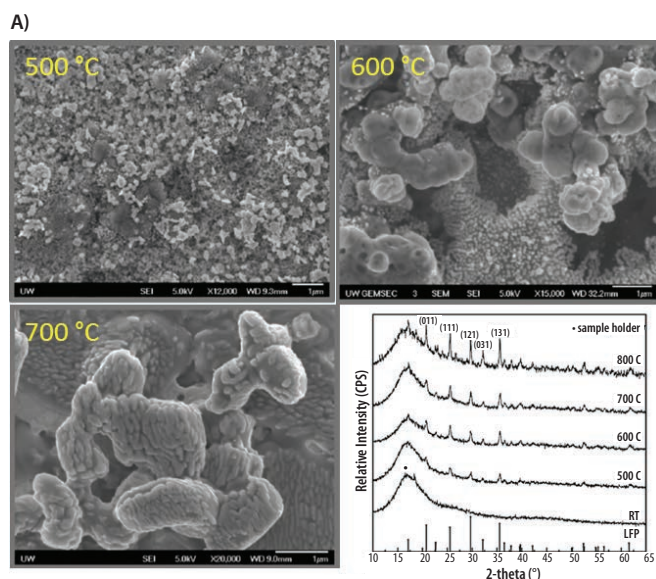
Figure 8. LiFePO$_4$/C nanocomposite for lithium ion battery. A) SEM images and XRD patterns and B) cyclic discharge capacities of LiFePO$_4$/C nanocomposite films annealed at different temperatures.[16]

Figure 8A shows a comparison of the cyclic discharge capacity of the LiFePO$_4$/C nanocomposite films annealed at different temperatures. Despite the high initial capacity, the sample annealed at 500 °C presented poor cyclic stability. The capacity dropped rapidly and reached 139 mAh/g after 13 cycles. This is attributed to the insufficient crystallinity of the film annealed at 500 °C. The best performance was achieved for samples annealed at 600 °C, which demonstrated the highest capacities of ~312 mAh/g for the initial cycle and approximately constant capacity of 218 mAh/g after 20 cycles. Annealing at higher temperatures, 700 °C and 800 °C, resulted in a significant decrease in capacity (228 mAh/g and

120 mAh/g for the initial cycle, dropping to 148 mAh/g and 99 mAh/g after 20 cycles). It is believed that 600 °C is the optimal temperature for annealing the LiFePO$_4$/C nanocomposite film because it gives rise to a slightly less crystallized/less compact structure that can accommodate more lithium ions and facilitate diffusion within the film.[16] Although films annealed at higher temperatures (e.g., 700 °C and 800 °C) possessed better crystallinity, their compact structure and decreased internal surface area delivered capacities lower than that of film annealed at 600 °C. This is also consistent with the trend observed with TiO$_2$ nanotube arrays produced with an anodization method discussed earlier.[6]

Conclusions and Remarks

Based on the above discussions, we can conclude that the capacity and cyclic stability of LIB technology rely heavily on the composition, morphology, crystal structure, and defects of the materials that form the electrode films. These parameters intrinsically affect the faradaic reaction occurring at solid–liquid interfaces and the electron/ion transport within batteries, and they are dependent on method of synthesis and post-treatment.

Internal Surface Area

Based on the results on MnO$_2$ nanowall arrays, TiO$_2$ nanotube arrays, V$_2$O$_5$ nanofibers, and V$_2$O$_5$ nanoporous films, it can be clearly seen that the morphology of materials, which primarily depends on the method of synthesis, plays a key role in determining the internal surface area. High surface area is usually the primary determinant of a material's performance in LIBs, as it allows for a large solid–liquid interface between the electrode films and electrolyte, enabling an efficient faradaic reaction. In addition to the synthesis method, which primarily determines the material's morphology, post-treatment such as annealing temperature and atmosphere also present an effective way to tailor the material's morphology. High internal surface area and the appropriate porosity benefit LIB performance by allowing the lithium ions to diffuse and to intercalate/deintercalate efficiently, contributing to high capacity.

Pathways for Electron and Ion Transport

The morphology of the materials used in batteries also influences the pathways of transport of electrons and lithium ions. In this aspect, 1D nanostructures present an obvious advantage over nanoparticles due to a significant reduction in the number of grain boundaries encountered during the electron or ion transport within electrode films. This makes the redox reaction in relation to lithium-ion intercalation and deintercalation more efficient, which allows batteries to be made with higher capacity. However, for electrode films with 1D nanomaterials, one usually needs to balance the trade-off between direct pathways for highly efficient transport and lower internal surface area provided by the 1D nanomaterials.

Crystallinity

Crystal structure or crystallinity is another issue closely related to the synthesis method and post-treatment. The use of amorphous materials for LIBs still seems to be up for debate. The MnO$_2$ nanowall arrays and TiO$_2$ nanotube arrays discussed above suggest amorphous materials may offer higher capacities compared to crystalline materials. This is because the relatively open structure of amorphous materials accommodates more lithium ions. However, as shown in the case of a TiO$_2$ nanotube, cyclic stability may be very poor for amorphous materials without heat treatment. It is generally observed that materials with better crystallinity possess better cyclic stability; whereas, higher capacity is achieved in less

well-crystallized materials. For example, for the LiFePO$_4$/C nanocomposites discussed above, the sample annealed at 600 °C demonstrated higher capacity than those annealed at 700 °C and 800 °C. In general, the crystallinity of a material is related to its electric conductivity. A less well crystallized material may contain some defects, such as oxygen vacancies, which lead to formation of an impurity energy level in the band gap and, therefore, lead to better conductivity than those perfectly crystallized materials. This enables higher capacity in a battery. It is worth pointing out that heat treatment at elevated temperatures not only reduces conductivity, it also causes the morphology to change. This usually corresponds to an increase in the size of crystallites and is a negative factor that diminishes the battery capacity due to a decrease in the internal surface area of the electrode film.

Defects

As mentioned above, the electric conductivity of the electrode film is related to its crystallinity via defect-induced impurity energy levels. The degree of defects formed in a material is affected by both the annealing temperature and the annealing atmosphere. It is shown that the use of CO and N$_2$ atmospheres during annealing of TiO$_2$ nanotubes and V$_2$O$_5$ xerogel films, respectively, introduces desired defects that result in the formation of low valence ions (e.g., Ti^{3+}, and V^{4+}, V^{3+}) and enhance the conductivity of electrode that leads to improvement in the battery capacity. The example of Mn-doped V$_2$O$_5$ film shows that in addition to controlling the annealing atmosphere, the use of a dopant during the material synthesis is also a way to introduce low valence ions and improve the battery performance.

References

(1) Johnson, C.; Dees, D.; Mansuetto, M.; Thackeray, M.; Vissers, D.; Argyriou, D.; Loong, C.-K.; Christensen, L. *Journal of power sources* **1997**, *68*, 570–577.
(2) Liu, D. W.; Zhang, Q. F.; Xiao, P.; Garcia, B. B.; Guo, Q.; Champion, R.; Cao, G. Z. *Chem. Mat.* **2008**, *20*, 1376–1380.
(3) Liu, D. W.; Garcia, B. B.; Zhang, Q. F.; Guo, Q.; Zhang, Y. H.; Sepehri, S.; Cao, G. Z. *Adv. Funct. Mater.* **2009**, *19*, 1015–1023.
(4) Mor, G. K.; Varghese, O. K.; Paulose, M.; Shankar, K.; Grimes, C. A. *Solar Energy Materials and Solar Cells* **2006**, *90*, 2011–2075.
(5) Roy, P.; Berger, S.; Schmuki, P. *Angewandte Chemie International Edition* **2011**, *50*, 2904–2939.
(6) Liu, D.; Xiao, P.; Zhang, Y.; Garcia, B. B.; Zhang, Q.; Guo, Q.; Champion, R.; Cao, G. *The Journal of Physical Chemistry C* **2008**, *112*, 11175–11180.
(7) Liu, D.; Zhang, Y.; Xiao, P.; Garcia, B. B.; Zhang, Q.; Zhou, X.; Jeong, Y.-H.; Cao, G. *Electrochimica Acta* **2009**, *54*, 6816–6820.
(8) Kim, D.; Ryu, H.; Moon, J.; Kim, J. *Journal of power sources* **2006**, *163*, 196–200.
(9) Fontenot, C. J.; Wiench, J. W.; Pruski, M.; Schrader, G. *The Journal of Physical Chemistry B* **2000**, *104*, 11622–11631.
(10) Liu, D.; Liu, Y.; Garcia, B. B.; Zhang, Q.; Pan, A.; Jeong, Y.-H.; Cao, G. *Journal of Materials Chemistry* **2009**, *19*, 8789–8795.
(11) Yu, D.; Zhang, S.; Liu, D.; Zhou, X.; Xie, S.; Zhang, Q.; Liu, Y.; Cao, G. *Journal of Materials Chemistry* **2010**, *20*, 10841–10846.
(12) Yu, D.; Chen, C.; Xie, S.; Liu, Y.; Park, K.; Zhou, X.; Zhang, Q.; Li, J.; Cao, G. *Energy & Environmental Science* **2011**, *4*, 858–861.
(13) Takahashi, K.; Wang, Y.; Cao, G. *The Journal of Physical Chemistry B* **2005**, *109*, 48–51.
(14) Wang, Y.; Cao, G. *Chem. Mat.* **2006**, *18*, 2787–2804.
(15) Liu, Y.; Clark, M.; Zhang, Q.; Yu, D.; Liu, D.; Liu, J.; Cao, G. *Advanced Energy Materials* **2011**, *1*, 194–202.
(16) Liu, Y.; Liu, D.; Zhang, Q.; Yu, D.; Liu, J.; Cao, G. *Electrochimica Acta* **2011**, *56*, 2559–2565.

Precursors for Lithium–ion Battery Materials Synthesis

Cobalt

For a complete list of available materials, visit aldrich.com/periodic.

Name	Composition	Purity	Form	Prod. No.
Cobalt(II) bromide, anhydrous	CoBr$_2$	99.99% trace metals basis	beads, −10 mesh	427136-1G 427136-5G
Cobalt(II) bromide	CoBr$_2$	99%	powder	334022-50G 334022-250G
Cobalt(II) carbonate hydrate	CoCO$_3$·xH$_2$O	99.99% trace metals basis	powder	379956-5G
Cobalt(II) chloride, anhydrous	CoCl$_2$	99.9% trace metals basis	beads, −10 mesh	449776-5G 449776-25G
Cobalt(II) chloride hydrate	CoCl$_2$·xH$_2$O, Degree of hydration 5-6	99.999% trace metals basis	powder and chunks	203084-10G
Cobalt(II) fluoride	CoF$_2$	-	powder	236128-25G
Cobalt(II) fluoride tetrahydrate	CoF$_2$·4H$_2$O	99.99% trace metals basis	powder	399876-5G
Cobalt(II) hydroxide, technical grade	Co(OH)$_2$	95%	powder	342440-250G
Cobalt(II) iodide, anhydrous	CoI$_2$	99.999%	powder	499129-1G
Cobalt(II) nitrate hexahydrate	Co(NO$_3$)$_2$·6H$_2$O	99.999% trace metals basis	crystals and lumps	203106-10G 203106-50G
Cobalt(II) oxalate dihydrate	CoC$_2$O$_4$·2H$_2$O	-	powder	401285-10G 401285-50G
Cobalt(II) perchlorate hexahydrate	Co(ClO$_4$)$_2$·6H$_2$O	-	crystals and lumps	401404-25G
Cobalt(II) sulfate hydrate	CoSO$_4$·xH$_2$O	99.998% trace metals basis	crystals and lumps	229598-10G

Iron

For a complete list of available materials, visit aldrich.com/periodic.

Name	Composition	Purity	Form	Prod. No.
Iron(II) bromide, anhydrous	$FeBr_2$	99.999% trace metals basis	beads, −10 mesh	434000-1G
Iron(III) bromide	$FeBr_3$	98%	powder	217883-10G 217883-50G
Iron(II) chloride, anhydrous	$FeCl_2$	99.998% trace metals basis	beads, −10 mesh	429368-1G 429368-10G
	$FeCl_2$	99.9% trace metals basis	beads, −10 mesh	450944-10G 450944-50G
Iron(II) chloride tetrahydrate	$FeCl_2 \cdot 4H_2O$	99.99% trace metals basis	crystals and lumps	380024-5G 380024-25G
Iron(III) chloride, anhydrous	$FeCl_3$	≥99.99% trace metals basis	powder	451649-1G 451649-5G
Iron(III) chloride, sublimed grade	$FeCl_3$	≥99.9% trace metals basis	powder or crystals	701122-1G 701122-5G 701122-25G
Iron(II) fluoride	FeF_2	98%	powder	399841-10G
Iron(III) fluoride	FeF_3	98%	powder	288659-10G
Iron(III) fluoride trihydrate	$FeF_3 \cdot 3H_2O$	-	powder	334499-25G
Iron(II) iodide, anhydrous	FeI_2	≥99.99% trace metals basis	beads, −10 mesh	400858-1G 400858-10G
Iron(III) nitrate nonahydrate	$Fe(NO_3)_3 \cdot 9H_2O$	≥99.999% trace metals basis	solid	529303-25G
Iron(II) oxalate dihydrate	$FeC_2O_4 \cdot 2H_2O$	99%	powder	307726-25G 307726-500G
Iron(III) oxalate hexahydrate	$Fe_2(C_2O_4)_3 \cdot 6H_2O$	-	powder and chunks	381446-5G 381446-25G
Iron(III) phosphate tetrahydrate	$FePO_4 \cdot 4H_2O$, Fe 24%	-	powder	436038-100G

Lithium

For a complete list of available materials, visit aldrich.com/periodic.

Name	Composition	Purity	Form	Prod. No.
Lithium bromide	LiBr	≥99.995% trace metals basis	powder and chunks	229733-25G 229733-125G
Lithium carbonate	Li_2CO_3	99.997% trace metals basis	powder	203629-10G 203629-50G
Lithium chloride	LiCl	≥99.99% trace metals basis	powder	203637-10G 203637-50G 203637-100G
Lithium fluoride	LiF	-	powder, -300 mesh	237965-100G 237965-1KG
Lithium hydroxide monohydrate	$LiOH \cdot H_2O$	99.95% trace metals basis	crystalline	254274-10G 254274-50G 254274-250G
Lithium iodide	LiI	99.9% trace metals basis	crystalline powder	518018-10G 518018-50G
Lithium nitrate	$LiNO_3$	99.99% trace metals basis	crystalline powder	229741-25G 229741-125G
Lithium phosphate	Li_3PO_4	-	powder	338893-100G
Lithium sulfate	Li_2SO_4	≥99.99% trace metals basis	solid	203653-10G

Manganese

For a complete list of available materials, visit aldrich.com/periodic.

Name	Composition	Purity	Form	Prod. No.
Manganese(II) chloride, anhydrous	$MnCl_2$	99.99% trace metals basis	beads, −10 mesh	429449-5G 429449-25G
Manganese(II) chloride	$MnCl_2$	≥99% trace metals basis	powder and chunks	244589-10G 244589-50G 244589-250G
Manganese(II) fluoride, anhydrous	MnF_2	99.99% trace metals basis	powder	771619-5G
Manganese(III) fluoride	MnF_3	99.9% trace metals basis	powder	339296-10G
Manganese(II) iodide, anhydrous	MnI_2	99.9%	powder	551619-1G
Manganese(II) nitrate hydrate	$Mn(NO_3)_2 \cdot xH_2O$, Degree of hydration 4-6	99.99% trace metals basis	crystals and lumps	203742-25G 203742-100G
Manganese(II) perchlorate hydrate	$Mn(ClO_4)_2 \cdot xH_2O$	99%	crystalline	359386-100G
Manganese(II) sulfate hydrate	$MnSO_4 \cdot xH_2O$	≥99.99% trace metals basis	solid	229784-25G 229784-100G

Nickel

For a complete list of available materials, visit aldrich.com/periodic.

Name	Composition	Purity	Form	Prod. No.
Nickel(II) acetate tetrahydrate	$Ni(OCOCH_3)_2 \cdot 4H_2O$	≥99.0%, KT	powder or crystals	72225-250G 72225-1KG
Nickel carbonate, basic hydrate	$NiCO_3 \cdot 2Ni(OH)_2 \cdot xH_2O$	99.9% trace metals basis	powder	544183-250G-A 544183-1KG-A
Nickel(II) chloride, anhydrous	$NiCl_2$	99.99% trace metals basis	powder	451193-5G 451193-25G
Nickel(II) chloride	$NiCl_2$	98%	powder	339350-50G 339350-250G
Nickel(II) chloride hexahydrate	$NiCl_2 \cdot 6H_2O$	99.999% trace metals basis	crystals and lumps	203866-5G 203866-25G
Nickel(II) hydroxide	$Ni(OH)_2$	-	powder	283622-250G 283622-1KG
Nickel(II) nitrate hexahydrate	$Ni(NO_3)_2 \cdot 6H_2O$	99.999% trace metals basis	solid	203874-20G 203874-100G 203874-500G
Nickel(II) sulfamate tetrahydrate	$Ni(SO_3NH_2)_2 \cdot 4H_2O$	98%	solid	262277-500G
Nickel(II) sulfate, anhydrous	$NiSO_4$	99.99% trace metals basis	solid	656895-10G 656895-50G
Nickel(II) sulfate heptahydrate	$NiSO_4 \cdot 7H_2O$	99.999% trace metals basis	crystals and lumps	203890-10G 203890-50G

Redi-Dri™ Free-flowing Powders

Never Chip, Chisel, or Grind Your Lab Reagents or Salts Again

Redi-Dri™ products eliminate clumping typically noted with many hygroscopic powders and provide free-flowing, ready-to-use materials every time. Don't waste money or time on salts that harden on the shelf. A nine-month study of the Redi-Dri™ Packaging System against standard packaging confirms:

The Redi-Dri™ packaging system prevents environmental water absorption and delivers a free-flowing powder every time!

Popular Redi-Dri™ Free-flowing Products

Prod. No.	Description
793639	Calcium chloride, anhydrous, free-flowing, Redi-Dri™, ACS reagent, ≥96% **NEW**
746487	Cesium chloride, anhydrous, free-flowing, Redi-Dri™, *ReagentPlus*®, 99.9%
746479	Lithium bromide, anhydrous, free-flowing, Redi-Dri™, *ReagentPlus*®, ≥99%
746460	Lithium chloride, anhydrous, free-flowing, Redi-Dri™, ACS reagent, ≥99%
746452	Magnesium sulfate, anhydrous, free-flowing, Redi-Dri™, *ReagentPlus*®, ≥99.5%
791733	Potassium acetate, anhydrous, free-flowing, Redi-Dri™, ACS reagent, ≥99%
746444	Potassium bromide, anhydrous, free-flowing, Redi-Dri™, ACS reagent, ≥99%
791776	Potassium carbonate, anhydrous, free-flowing, Redi-Dri™, ACS reagent, ≥99%
746436	Potassium chloride, anhydrous, free-flowing, Redi-Dri™, ACS reagent, ≥99%
746428	Potassium iodide, anhydrous, free-flowing, Redi-Dri™, ACS reagent, ≥99%
791741	Sodium acetate, anhydrous, free-flowing, Redi-Dri™, ACS reagent, ≥99%
792519	Sodium bicarbonate, anhydrous, free-flowing, Redi-Dri™, ACS reagent, ≥99.7% **NEW**
793574	Sodium bromide, anhydrous, free-flowing, Redi-Dri™, ACS reagent, ≥99% **NEW**
791768	Sodium carbonate, anhydrous, free-flowing, Redi-Dri™, ACS reagent, ≥99.5%
746398	Sodium chloride, anhydrous, free-flowing, Redi-Dri™, ACS reagent, ≥99%
746371	Sodium iodide, anhydrous, free-flowing, Redi-Dri™, ACS reagent, ≥99.5%
746363	Sodium sulfate, anhydrous, free-flowing, Redi-Dri™, ACS reagent, ≥99%
746355	Zinc chloride, anhydrous, free-flowing, Redi-Dri™, ACS reagent, ≥97%

For a full listing of the Red-Dri™ product line and additional information, visit
sigma-aldrich.com/redi-dri-matters

SCALING UP HIGH–ENERGY CATHODE MATERIALS FOR ELECTRIC VEHICLES

Young Ho Shin, Ozgenur Kahvecioglu Feridun, Gregory Krumdick
Materials Engineering Research Facility, Energy Systems Division, Argonne National Laboratory
9700 S. Cass Avenue, Argonne, IL, 60439
Email: gkrumdick@anl.gov

This article details the process development and scale up of $Li_{1.14}Ni_{0.29}Mn_{0.57}O_2$, one of several promising cathode materials developed at bench-scale at Argonne National Laboratory for use in electric vehicle applications. The process developed is reproducible and produces high quality material for further research and evaluation, including formation mechanism studies, surface coating, and pouch-cell testing. The precursor of this lithium and manganese-rich metal oxide material was produced using carbonate co-precipitation, which produced spherical particles, prohibited the oxidation of Mn^{2+} to Mn^{3+}, and kept the oxidation state of all transition metals as $2+$.[5-6] The article also elaborates on the electrochemical properties of the scaled-up material.

Introduction

The critical technical challenges associated with the commercialization of electric vehicle batteries include cost, performance, abuse tolerance, and lifespan. Selection of optimal active cathode material is a critical factor in determining both the performance and the materials cost of an electric vehicle battery. For this reason, many research groups are developing advanced cathode materials in order to reduce the cost, volume, and weight of the cathode material in each battery.[1] Recently developed cathode materials, lithium and manganese-rich metal oxides (LMR-NMC), are a promising material class with energy densities over 200 mAh/g and the potential to lower the cost of electric vehicle batteries.

At the research stage, new materials are typically synthesized and tested at gram quantities. However, the consistency and performance of these materials when produced in large batch sizes remains uncertain until the synthesis process has been developed. Industry is typically reluctant to take on the financial risk of process scale-up for untested materials. Hence, process development and scale-up of advanced battery materials is the critical link connecting material discovery, market evaluation, and high-volume manufacturing.[2–4] To bridge research and commercialization of high-energy cathode materials, systematic engineering research is ongoing at Argonne's Materials Engineering Research Facility (MERF). This involves investigating customized synthesis and scale-up of each candidate material via several reaction techniques including high energy ball milling, carbonate and hydroxide co-precipitation, and other next-generation reaction techniques. By these synthesis methods, we have scaled up numerous precursor and cathode materials, including $Ni_{0.33}Mn_{0.67}CO_3$, $MnCO_3$, $Ni_{0.16}Mn_{0.67}Co_{0.16}CO_3$, $Ni_{0.33}Mn_{0.67}(OH)_2$, $Ni_{0.27}Mn_{0.54}Co_{0.19}(OH)_2$, Li_2MnO_3, and $Li_{1.14}Ni_{0.29}Mn_{0.57}O_2$.

Synthesis Method

To produce kilogram quantities of high-energy lithium and manganese-rich cathode materials (specifically, $Li_{1.14}Ni_{0.29}Mn_{0.57}O_2$), we first used the co-precipitation method to synthesize the initial carbonate precursors ($Ni_{0.33}Mn_{0.67}CO_3$). Nickel sulfate hexahydrate ($NiSO_4 \cdot 6H_2O$, **Sigma-Aldrich Prod. No. 227676**) and manganese sulfate monohydrate ($MnSO_4 \cdot H_2O$, **Sigma-Aldrich Prod. No. M7634**) were used as starting raw materials to prepare the transition metal aqueous solution with a concentration of 1 M. The feed flow rates of the transition metal aqueous solution, sodium carbonate (**Sigma-Aldrich Prod. No. S7795**) solution, and ammonium hydroxide solution (**Sigma-Aldrich Prod. No. 320145**) were carefully determined and controlled to keep the pH value of co-precipitation at 8.0 ± 0.1. During co-precipitation, precursor materials were collected every 30 min to measure particle growth, morphology, and size distribution. The obtained precursor products were filtered, washed, and dried in a vacuum oven at 40 °C for 24 hr. Finally, the dried precursor particles were mixed thoroughly with Li_2CO_3 (**Sigma-Aldrich Prod. No. 255823**) and then calcined at 900 °C.

The electrochemical properties of the obtained materials were evaluated with coin-type half-cells (CR2032). To prepare the positive electrode, 84 wt.% active material, 8 wt.% super C65 carbon black, and 8 wt.% PVDF in NMP were mixed and coated onto an aluminum foil. The thickness of the cathode film was ~40 μm. Celgard 2325 membrane was used as the separator, and the electrolyte was 1.2 M $LiPF_6$ dissolved in the ethylene carbonate and ethyl methyl carbonate in a ratio of 3:7 (wt.%).

For questions, product data, or new product suggestions, contact us at **matsci@sial.com**.

131

Development of a Continuous Co-precipitation Process

A scalable and economically feasible continuous synthesis process is critical for both commercialization and optimal quality control in the production of cathode materials. Steady-state production by continuous co-precipitation means that product properties such as precursor size, morphology, size distribution and particle density are consistent throughout the operation time. Therefore, continuous co-precipitation provides superior consistency in product quality with low manufacturing cost, which is a key factor for the performance and cost of battery packs.

For a conventional continuous stirred-tank reactor (CSTR) system, the growth of particles is uncontrollable and results in relatively large particles over 30 μm, triggering detrimental effects on battery safety and performance.[6] This is due to the contribution of too many conjugated process variables including reactor geometry, reaction temperature, reaction medium pH, residence time, feed concentration, feed flow rate, stirring speed, and impeller type, among other factors. These inputs have a strong impact on nucleation, particle growth, morphology, and density. Even though a CSTR system has product consistency and economic feasibility, the product properties themselves can be very hard to control compared to batch processes. Therefore, it is quite challenging to produce a precursor within the desired specification via a continuous operation. By systematic process engineering research at Argonne's MERF, an advanced 20L CSTR system was developed to produce a spherical and size-controlled carbonate precursor by a co-precipitation method.

Figures 1A and **1B** show typical precursor growth tendencies during 30 hr co-precipitation to produce a carbonate precursor using an advanced 20L CSTR system invented at Argonne's MERF. The particle size of the precursor increases slowly in the early stage of co-precipitation which is an unsteady-state region. When the steady-state region begins at 25 hr operation, the particle size, morphology, size distribution, and density of the precursor remain constant over time. As shown in **Figure 1A**, the average particle size (D50) of slurry product is stable, and the precursor particles do not grow further under steady-state conditions.
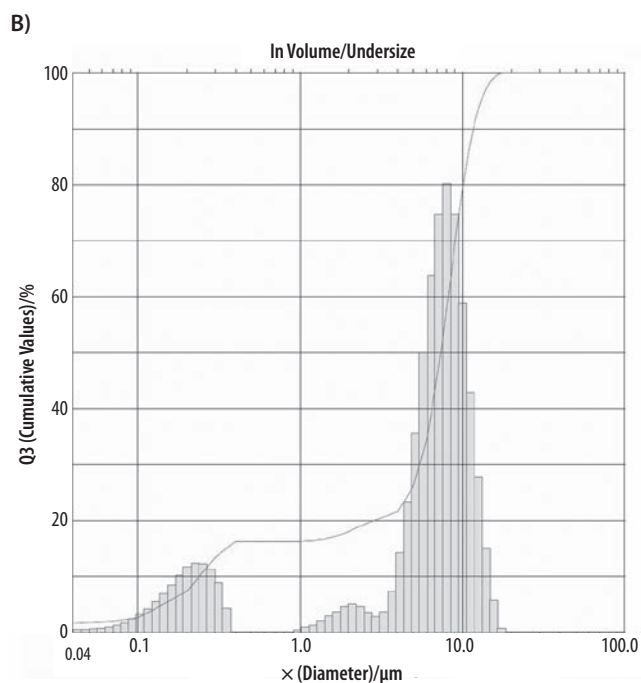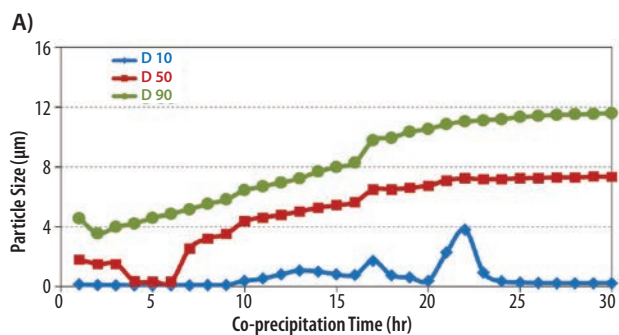
Figure 1. A) Unsteady-state precursor growth (0–25 hr) and steady-state precursor production (25–30 hr). B) Particle size analysis of precursor slurry at 30 hr co-precipitation.

Figure 2 shows typical Scanning Electron Microscopy (SEM) images of $Ni_{0.33}Mn_{0.67}CO_3$ carbonate precursors obtained at the steady-state conditions. The average particle size was found to be 7 μm, which is consistent with the particle size analysis results given in **Figure 1**. The micrograph also reveals the precursor particles have slightly quasi-spherical morphologies with a smooth surface.
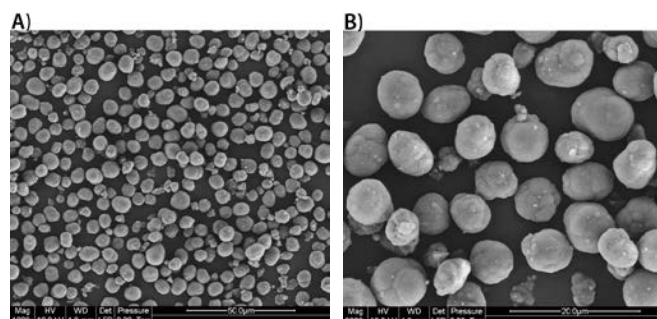
Figure 2. SEM microscopy of the dried $Ni_{0.33}Mn_{0.67}CO_3$ precursor collected during steady-state co-precipitation (25–30 hr).

Scaling Up High-energy Cathode ($Li_{1.14}Ni_{0.29}Mn_{0.57}O_2$) Materials

Cobalt-free lithium and manganese-rich metal oxides are attractive cathode materials because of their high-energy density. For electric vehicle applications, the $Li_{1.14}Ni_{0.29}Mn_{0.57}O_2$ compound was selected as a scale-up material. Its precursor ($Ni_{0.33}Mn_{0.67}CO_3$) was produced by a customized 20L CSTR co-precipitation system. The physical properties of the precursor (such as particle size, morphology, size distribution, and density) have a strong effect on the electrochemical performance of the cathode materials.[7–9] Therefore, we optimized synthesis conditions of this precursor in order to maximize performance.

Figure 3 shows SEM images of the spherical $Li_{1.14}Ni_{0.29}Mn_{0.57}O_2$ cathode material which has a porous structure and a surface area of 3.9 m^2g^{-1}. However, as seen in **Figure 2**, the precursor surface is smoother but has a surface area of 176.5 m^2g^{-1}. This indicates the precursor is composed of nanosized primary particles produced by carbonate co-precipitation. These nanosized primary particles mix with the lithium source and become larger primary particles during the calcination step at 900 °C.
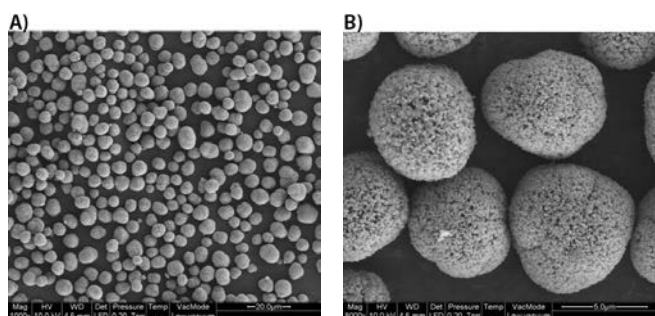
Figure 3. SEM images of the scaled-up $Li_{1.14}Ni_{0.29}Mn_{0.57}O_2$.

X-ray diffraction (XRD) studies were conducted to further investigate the phases formed after lithiation. The XRD pattern in **Figure 4** shows the existence of a secondary component between 20° and 25° (Li_2MnO_3-like phase) in the structure of $Li_{1.14}Ni_{0.29}Mn_{0.57}O_2$. This can be primarily indexed based on the m space group with a typical hexagonal structure and a major layered component as in similar materials.[10–11] The clear peak splits in preferred orientation is also shown in the XRD profile, indicating a well-defined crystallization of the material.

Figure 5 shows the first and second charge–discharge profile of $Li_{1.14}Ni_{0.29}Mn_{0.57}O_2$. The current density was equivalent to C/10, assuming that 250 mAh g^{-1} is achieved at the 1 C rate and the cell cycled between 2.0 V and 4.75 V. The first discharge capacity of scaled-up material is 250 mAh g^{-1}, with a columbic efficiency of 83.9%. This capacity is higher than that of the bench-scale material (229 mAh g^{-1}). The second discharge capacity of scale-up material is 248 mAh g^{-1}.
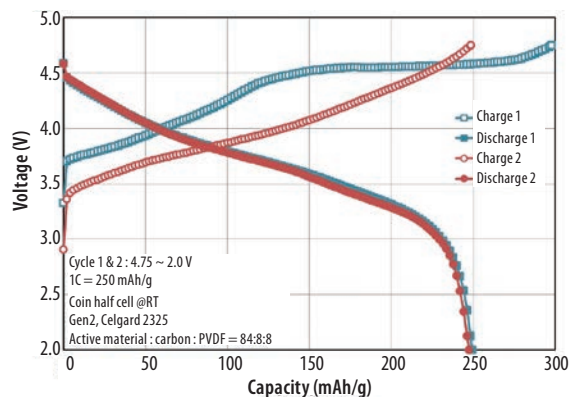
Figure 5. First and second charge–discharge profile of $Li_{1.14}Ni_{0.29}Mn_{0.57}O_2$.

Figure 6A presents the cyclic performance comparison between the bench-scale and scaled-up $Li_{1.14}Ni_{0.29}Mn_{0.57}O_2$. The initial two charge–discharge cycles were obtained between 2.4 V and 4.75 V under C/10 rate; the current density was equivalent to C/3 between 2.4 V and 4.5 V for the subsequent cycles. The scaled-up material shows high discharge capacity and excellent cycling performance retaining a capacity of 180 mAh g^{-1} after 140 cycles at C/3 rate. As shown in **Figure 6B**, the rate capability of the scaled-up material is much better than that of the bench-scale material at the C rates of C/10, C/5, C/3, C/2, 1 C, 2 C, 3 C, 4 C, and 5 C. This comparison suggests that the smaller size and narrower size distribution

Figure 4. X-ray diffraction pattern of $Li_{1.14}Ni_{0.29}Mn_{0.57}O_2$.

of the particles comprising the scaled-up material, compared to those of the bench-scale material, increase the rate capability of $Li_{1.14}Ni_{0.29}Mn_{0.57}O_2$. The scaled-up $Li_{1.14}Ni_{0.29}Mn_{0.57}O_2$ delivers a high discharge capacity and shows superior cycle stability and rate performance.

A)

Cycle 1 & 2 : 4.75 ~ 2.4, C/10
Cycle 3 ~ 140 : 450 ~ 2.4 V, C/3
1C = 250 mAh/g
Coin half cell @RT
Gen2, Celgard 2325
Active material : carbon : PVDF = 84:8:8

B)

Cycle 1 ~ 5 : 4.75 ~ 2.4 V
Cycle 6 ~ 45 : 450 ~ 2.4 V
1C = 250 mAh/g
Coin half cell @RT
Gen2, Celgard 2325
Active material : carbon : PVDF = 84:8:8
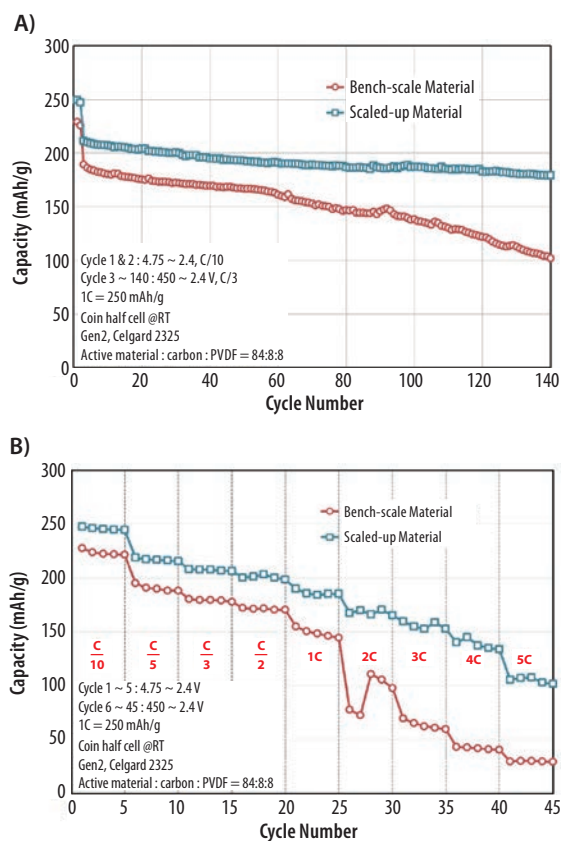
Figure 6. A) Cycling and **B)** rate performance comparison between the bench-scale and scaled-up materials of $Li_{1.14}Ni_{0.29}Mn_{0.57}O_2$.

Summary

The results of 30 hr co-precipitation clearly showed that the developed 20L CSTR system generates 7 µm spherical precursor continuously, and we have successfully scaled up high-energy cathode materials to kilogram quantities. Since the electrochemical performance of a cathode material (capacity, energy density, cycle life, etc.) is strongly affected by the synthesis and scale-up methodology, developing a customized synthesis process for target bench-scale cathode materials while maintaining economic feasibility is critical for the battery industry. This process development and scale-up research is a major stepping stone between the research lab and the commercialization of high-energy materials that will be used in electric vehicles.

Acknowledgments

References
(1) Xu, B.; Qian, D.; Wang, Z.; Meng, Y.S. *Mater. Sci. Eng., R* **2012**, *73*, 51.
(2) Cheng, F.; Xin, Y.; Chen, J.; Lu, L.; Zhang, X.; Zhou, H. *J. Mater. Chem. A* **2013**, *1*, 5301.
(3) Scrosati, B.; Garche, J. *J. Power Sources* **2010**, *195*, 2419.
(4) Brodd, R.J.; Helou, C. *J. Power Sources* **2013**, *231*, 293.
(5) Lee, D.K.; Park, S.H.; Amine, K.; Bang, H.J.; Parakash, J.; Sun, Y.K. *J. Power Sources* **2006**, *162*, 1346.
(6) Wang, D.; Belhaourak, I.; Koening, G.M.; Zhou, G.; Amine, K. *J. Mater. Chem.* **2011**, *21*, 9290.
(7) Lee, K.S.; Myung, S.T.; Moon, J.S.; Sun, Y.K. *Electrochim. Acta* **2008**, *53*, 6033.
(8) Lee, M.H.; Kang, Y.J.; Myung, S.T.; Sun, Y.K. *Electrochim. Acta* **2004**, *50*, 939.
(9) Noh, M.; Cho, J. *J. Electrochem. Soc.* **2013**, *160* (1), A105.
(10) He, P.; Yu, H.; Li, D.; Zhou, H. *J. Mater. Chem.* **2012**, *22*, 3680.
(11) Thackeray, M.M.; Kang, S.H.; Johnson, C.S.; Vaughey, J.T.; Benedek, R.; Hackney, S.A. *J. Mater. Chem.* **2007**, *17*, 3112.

Electrode Materials

Electrode Sheets

For a complete list of available materials, visit aldrich.com/lib.

Name	Composition	Purity	Nominal Voltage (V)	Capacity (minimum)	Capacity (nominal)	Prod. No.
Lithium manganese nickel oxide, LMNO	$Li_2Mn_3NiO_8$	≥98%	4.7 (Li/Li$^+$)	125 mAh/g	115 mAh/g	765198-1EA
Lithium manganese oxide, LMO	$LiMn_2O_4$	≥98%	4.7 (Li/Li$^+$)	120 mAh/g	110 mAh/g	765201-1EA
Lithium nickel cobalt aluminium oxide, NCA	$LiNi_{0.8}Co_{0.15}Al_{0.05}O_2$	≥98%	3.7 (Li/Li$^+$)	150 mAh/g	180 mAh/g	765171-1EA
Lithium nickel manganese cobalt oxide, NMC	$LiNi_{0.33}Mn_{0.33}Co_{0.33}O_2$	-	3.5 (Li/Li$^+$)	210 mAh/g	-	765163-1EA
Lithium titanate, LTO	$Li_4Ti_5O_{12}$	≥98%	1.5 (Li/Li$^+$)	150 mAh/g	160 mAh/g	765155-1EA

Cathode Materials

For a complete list of available materials, visit aldrich.com/lib.

Name	Composition	Particle Size	Description	Prod. No.
Cobalt monoantimonide	CoSb	-80 mesh	99.9% trace metals basis	746320-5G
Lithium cobalt(III) oxide	$LiCoO_2$	-	powder, 99.8% trace metals basis	442704-100G-A
Lithium cobalt phosphate, LCP	$LiCoPO_4$	-	powder, 99%	725145-25G
	$LiCoPO_4$	-	powder, 99.9% trace metals basis	777110-25G
Lithium iron(III) oxide	$LiFeO_2$	particle size <1 μm	powder, 95%	442712-100G-A
Lithium iron(II) phosphate, LFP	$LiFePO_4$	particle size <5 μm (BET)	powder, >97% (XRF)	759546-5G
Lithium manganese dioxide	$LiMnO_2$	particle size <1 μm	powder, >99% trace metals basis	725137-25G
Lithium manganese nickel oxide, LMNO	$Li_2Mn_3NiO_8$	particle size <0.5 μm (BET)	powder, >99%	725110-25G
Lithium manganese oxide, LMO	$LiMn_2O_4$	particle size <0.5 μm (BET)	powder, >99%	725129-25G
Lithium manganese(III,IV) oxide, LMO	$LiMn_2O_4$	particle size <5 μm	-	482277-25G
Lithium molybdate	Li_2MoO_4	-	powder or crystals, 99.9% trace metals basis	400904-250G
Lithium nickel cobalt aluminium oxide, NCA	$LiNi_{0.8}Co_{0.15}Al_{0.05}O_2$	particle size <0.5 μm	powder, >98%	760994-10G
Lithium nickel cobalt oxide, LNCO	$LiNi_{0.8}Co_{0.2}O_2$	particle size <0.5 μm	powder, >98%	760986-10G
Lithium nickel dioxide, LNO	$LiNiO_2$	particle size <3 μm (BET)	powder, ≥98% trace metals basis	757365-10G
Lithium nickel manganese cobalt oxide, NMC	$LiNi_{0.33}Mn_{0.33}Co_{0.33}O_2$	particle size <0.5 μm	powder, >98%	761001-10G
Manganese nickel carbonate	$Mn_{0.75}Ni_{0.25}CO_3$	-	powder, 99.99% trace metals basis (excluding Mg)	763608-25G

Anode Materials

For a complete list of available materials, visit aldrich.com/lib.

Name	Purity	Description	Form	Prod. No.
Lithium	99%, metals basis	particle size 4-10 mesh	granular	444456-10G 444456-50G
	99.9% trace metals basis	thickness × W 1.5 × 100 mm	ribbon	266000-25G 266000-100G
	99.9% trace metals basis	thickness × W 0.75 × 45 mm	ribbon	265993-25G 265993-100G
	99.9% trace metals basis	thickness × W 0.75 × 19 mm	ribbon	320080-25G 320080-100G
	99.9% trace metals basis	thickness × W 0.38 × 23 mm	ribbon	265985-25G 265985-100G
	≥98%	diam. 3.2 mm	wire	278327-25G 278327-100G
Lithium-aluminum alloy	-	-	powder	426490-25G
Lithium titanate, LTO	-	−325 mesh	powder	400939-100G
Lithium titanate, spinel, LTO nanopowder	>99%	particle size <200 nm (BET)	nanopowder	702277-25G
Tin(IV) oxide	-	particle size <100 nm (BET)	nanopowder	549657-5G 549657-25G

Electrolyte Solutions

For a complete list of available materials, visit aldrich.com/lib.

Name	Solvent	Prod. No.
1.0 M LiPF$_6$ in EC/DMC=50/50 (v/v)	in ethylene carbonate and dimethyl carbonate	746711-100ML
1.0 M LiPF$_6$ in EC/EMC=50/50 (v/v)	in ethylene carbonate and ethyl methyl carbonate	746738-100ML
1.0 M LiPF$_6$ in EC/DEC=50/50 (v/v)	in ethylene carbonate and diethyl carbonate	746746-100ML
1.0 M LiPF$_6$ in DMC	in dimethyl carbonate	746754-100ML
1.0 M LiPF$_6$ in EMC	in ethyl methyl carbonate	746762-100ML
1.0 M LiPF$_6$ in DEC	in diethyl carbonate	746770-100ML
1.0 M LiPF$_6$ in PC	in propylene carbonate	746789-100ML

Solvents and Additives

For a complete list of available materials, visit aldrich.com/lib.

Name	Structure	Purity	Prod. No.
Acetonitrile, ACN	CH_3CN	99.999% trace metals basis	733466-1L 733466-4L
Allyl methyl sulfone, MAS		96%	718203-5G
Bis(trifluoromethane)sulfonimide lithium salt		-	449504-10G 449504-50G
1-Butyl-3-methylimidazolium methanesulfonate		99.9% trace metals basis	724394-5G
1-Butyl-3-methylimidazolium thiocyanate		≥95%	724408-5G
Diethyl carbonate		≥99%	517135-100ML 517135-1L
Diethyl sulfite, DES		98%	774278-25G
Dimethyl carbonate, DMC		≥99%	517127-100ML 517127-1L 517127-2L 517127-20L
1,2-Dimethyl-3-propylimidazolium bis(trifluoromethylsulfonyl)imide, DMPIIm		99.9% trace metals basis	724416-1G
Ethylene sulfite, ES		≥99.0%	774251-25G
Ethyl methyl carbonate, EMC		99%	754935-50ML
1-Ethyl-3-methylimidazolium tetrachloroaluminate		99.9% trace metals basis	724424-5G
Ethyl methyl sulfone		97%	709980-5G
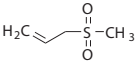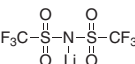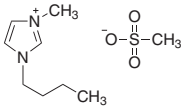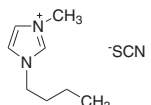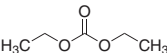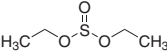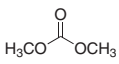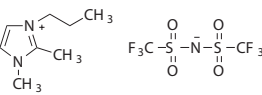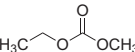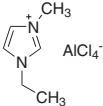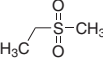
Name	Structure	Purity	Prod. No.
Fluoroethylene carbonate, FEC		99%	757349-25G
Lithium aluminum titanium phosphate, LATP	$Li_{1.3}Al_{0.3}Ti_{1.7}(PO_4)_3$	≥99.9% trace metals basis	790516-10G
Lithium bis(oxalato)borate, LiBOB	$LiB(C_2O_4)_2$	-	757136-25G
Lithium difluoro(oxalato)borate, LIODFB; LIF2OB; LIFOB	$LiBF_2(C_2O_4)$	99%	774138-25G
Lithium perchlorate	$LiClO_4$	99.99% trace metals basis	634565-10G 634565-100G
3-(Methylsulfonyl)-1-propyne		95%	718319-5G
Methyl-trioctylammonium bis(trifluoromethylsulfonyl)imide		99.9% trace metals basis	724432-1G
Phosphoric acid	H_3PO_4	≥99.999% trace metals basis	452289-50ML 452289-250ML
Propylene carbonate		99.7%	310328-100ML 310328-500ML 310328-1L 310328-2L
1,2-Propyleneglycol sulfite, PS		≥98%	774456-10G
Propylene sulfate		≥99%	774294-10G
1,3-Propylene sulfite, TMS; PS		99.5%	774243-25G
Vinylene carbonate, VC		99%	757144-25G
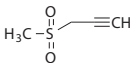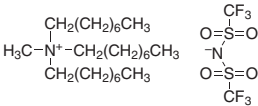
MAKE YOUR OWN
LITHIUM-ION
BATTERIES

Applications of lithium-ion batteries (LIBs) extend from modern electronics to automobiles. Order ready-to-use electrolyte solutions and electrode sheets in battery grade to fabricate your LIB.
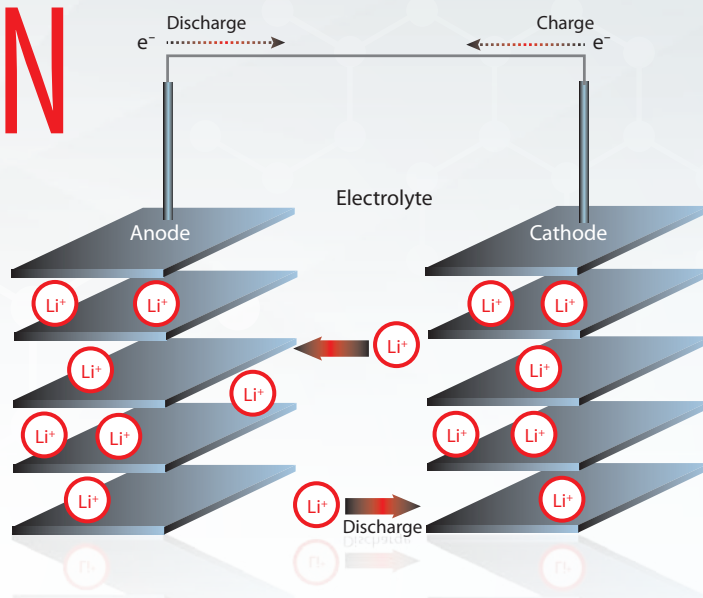
Electrolyte Solutions

Name	Specifications	Prod. No.
1.0 M LiPF$_6$ in EC/DMC=50/50 (v/v)	in ethylene carbonate and dimethyl carbonate, battery grade	746711
1.0 M LiPF$_6$ in EC/EMC=50/50 (v/v)	in ethylene carbonate and ethyl methyl carbonate, battery grade	746738
1.0 M LiPF$_6$ in EC/DEC=50/50 (v/v)	in ethylene carbonate and diethyl carbonate, battery grade	746746
1.0 M LiPF$_6$ in DMC	in dimethyl carbonate, battery grade	746754
1.0 M LiPF$_6$ in EMC	in ethyl methyl carbonate, battery grade	746762
1.0 M LiPF$_6$ in DEC	in diethyl carbonate, battery grade	746770
1.0 M LiPF$_6$ in PC	in propylene carbonate, battery grade	746789

Electrode Sheets

Name	Specifications	Composition	Prod. No.
Lithium nickel manganese cobalt oxide	aluminum substrate, size 5 in. × 10 in, loading >80%, thickness 25-50 μm	LiNi$_{0.33}$Mn$_{0.33}$Co$_{0.33}$O$_2$	765163
Lithium nickel cobalt aluminum oxide	aluminum substrate, size 5 in. × 10 in, loading >80%, thickness 12-25 μm	LiNi$_{0.8}$Co$_{0.15}$Al$_{0.05}$O$_2$	765171
Lithium manganese nickel oxide	aluminum substrate, size 5 in. × 10 in, loading >80%, thickness 25-50 μm	Li$_2$Mn$_3$NiO$_8$	765198
Lithium manganese oxide	aluminum substrate, size 5 in. × 10 in, loading >80%, thickness 25-40 μm	LiMn$_2$O$_4$	765201
Lithium titanate spinel	aluminum substrate, size 5 in. × 10 in, loading >80%, thickness 25-50 μm	Li$_4$Ti$_5$O$_{12}$	765155

For a complete list of LIB materials, including electrode powders, electrolytes, solvents and additives, visit **aldrich.com/lib**